Cell Reports

Article

AMPK regulates Bcl2-L-13-mediated mitophagy induction for cardioprotection

Graphical abstract

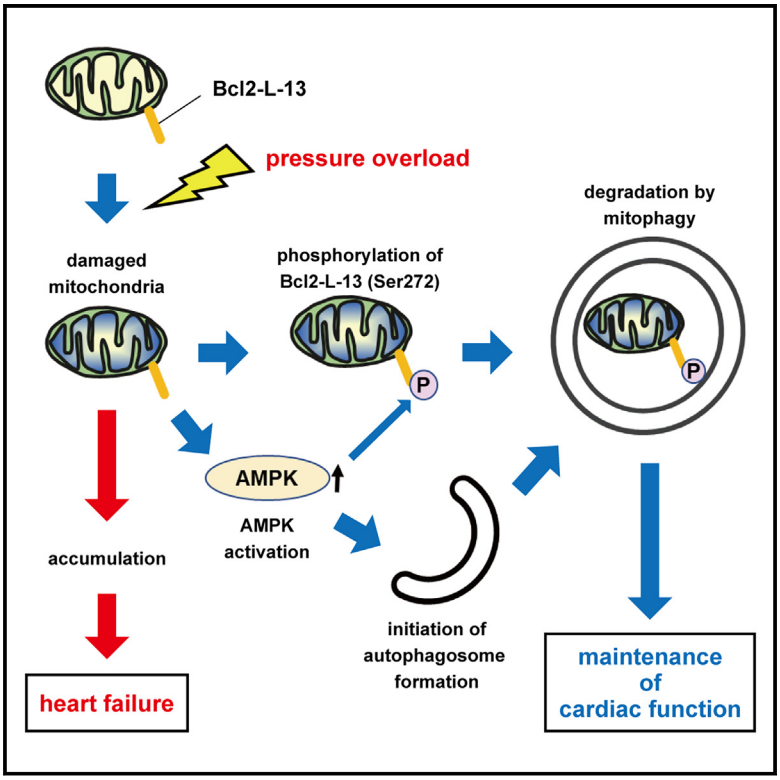

Highlights

- Bcl2-L-13 plays a protective role in the pressure-overloaded heart
- Bcl2-L-13 is involved in mitophagy and mitochondrial fission *in vivo*
- AMPKα2 is the responsible kinase to phosphorylate Bcl2-L-13 at Ser272

Authors

Tomokazu Murakawa, Jumpei Ito, Mara-Camelia Rusu, ..., Osamu Yamaguchi, Yasushi Sakata, Kinya Otsu

Correspondence

otsu.kinya@ncvc.go.jp

In brief

Murakawa et al. demonstrate that pressure overload to the heart induces Bcl2-L-13-mediated mitochondrial fission and mitophagy. Furthermore, its activation by phosphorylation is essential for maintaining cardiac function. The kinase library screening revealed that AMPKα2 is the responsible kinase. These findings elucidate the cardioprotective role of Bcl2-L-13.

Murakawa et al., 2024, Cell Reports *43*, 115001
December 24, 2024
https://doi.org/10.1016/j.celrep.2024.115001

CellPress

Cell Reports

CellPress
OPEN ACCESS

Article

AMPK regulates Bcl2-L-13-mediated mitophagy induction for cardioprotection

Tomokazu Murakawa,[1,2] Jumpei Ito,[2,3] Mara-Camelia Rusu,[2] Manabu Taneike,[1,2] Shigemiki Omiya,[2,3] Javier Moncayo-Arlandi,[2] Chiaki Nakanishi,[2,3] Ryuta Sugihara,[1] Hiroki Nishida,[1] Kentaro Mine,[1] Roland Fleck,[4,5] Min Zhang,[2] Kazuhiko Nishida,[2] Ajay M. Shah,[2] Osamu Yamaguchi,[3,6] Yasushi Sakata,[1] and Kinya Otsu[2,3,7,*]

[1]Department of Cardiovascular Medicine, Osaka University Graduate School of Medicine, 2-2 Yamadaoka, Suita, Osaka 565-0871, Japan
[2]The School of Cardiovascular Medicine and Sciences, King's College London British Heart Foundation Centre of Excellence, 125 Coldharbour Lane, SE5 9NU London, UK
[3]National Cerebral and Cardiovascular Center, 6-1 Kishibe-Shimmachi, Suita, Osaka 564-8565, Japan
[4]Centre for Ultrastructural Imaging, New Hunts House, King's College London, SE1 1UL London, UK
[5]Randall Centre for Cell and Molecular Biophysics, King's College London, SE1 1UL London, UK
[6]Department of Cardiology, Pulmonology, Hypertension & Nephrology, Ehime University Graduate School of Medicine, 454 Shitsukawa, Toon, Ehime 791-0295, Japan
[7]Lead contact
*Correspondence: otsu.kinya@ncvc.go.jp
https://doi.org/10.1016/j.celrep.2024.115001

SUMMARY

The accumulation of damaged mitochondria in the heart is associated with heart failure. Mitophagy is an autophagic degradation system that specifically targets damaged mitochondria. We have reported previously that Bcl2-like protein 13 (Bcl2-L-13) mediates mitophagy and mitochondrial fission in mammalian cells. However, the *in vivo* function of Bcl2-L-13 remains unclear. Here, we demonstrate that Bcl2-L-13-deficient mice and knockin mice, in which the phosphorylation site (Ser272) on Bcl2-L-13 was changed to Ala, showed left ventricular dysfunction in response to pressure overload. Attenuation of mitochondrial fission and mitophagy led to impairment of ATP production in these mouse hearts. In addition, we identified AMPKα2 as the kinase responsible for the phosphorylation of Bcl2-L-13 at Ser272. These results indicate that Bcl2-L-13 and its phosphorylation play an important role in maintaining cardiac function. Furthermore, the amplitude of stress-stimulated mitophagic activity could be modulated by AMPKα2.

INTRODUCTION

Heart failure is a major cause of morbidity and mortality despite advances in its management.[1] Mitochondria are abundant in energy-demanding cardiac tissue, and defects in mitochondrial structure and function are associated with heart failure.[2] Under pathological conditions, clearance of dysfunctional mitochondria is critical for maintaining the homeostasis of cardiomyocytes.[3] Autophagy is a highly conserved process of protein and organelle degradation in response to nutrient shortages and cytotoxic insults.[4] While autophagy nonselectively sequesters its cargos, selective degradation of damaged mitochondria relies on an autophagy-related transport system: mitophagy. In yeast, the Atg32 protein plays an essential role in mitophagy.[5,6] In mammalian cells, several types of mitophagy receptors or receptor-related factors, including NIP3-like protein X (NIX), BCL2/adenovirus E1B 19 kDa protein-interacting protein 3 (BNIP3), FUN14 domain containing 1 (FUNDC1), and phosphatase and tensin homolog-induced putative kinase protein 1 (PINK1)/Parkin have been reported.[7] We have previously identified Bcl2-L-13 as a functional mammalian homolog of Atg32.[8] Bcl2-L-13 induces both mitochondrial fission and mitophagy through its binding with microtubule-associated protein 1A- or 1B-light chain 3B (LC3B) in HEK293 cells. Phosphorylation and dephosphorylation serve as regulatory mechanisms to modulate the activity of mitophagy-related molecules.[9–12] We have also previously reported that phosphorylation of Ser272 on Bcl2-L-13 results in the enhancement of mitophagic activity.[8] However, the kinase responsible for this phosphorylation has not been identified. Furthermore, the *in vivo* function of Bcl2-L-13 in the heart is poorly understood.

The heart is an organ that demonstrates high mRNA expression levels of Bcl2-L-13.[13] Therefore, this study aimed to determine the *in vivo* functional role of Bcl2-L-13 in cardiac function. For this, we generated Bcl2-L-13-deficient mice. The mice showed attenuation of pressure overload-induced mitochondrial fission and mitophagy to protect the heart against pressure overload. In addition, analyses on knockin mice, in which the phosphorylation site Ser272 was changed to Ala (*Bcl2l13*$^{S272A/S272A}$), indicated that the activation of Bcl2-L-13 by its phosphorylation at Ser272 is essential for maintaining mitochondrial dynamics and cardiac function under pressure overload. Furthermore, screening of the kinase library revealed that 5′-AMP-activated

protein kinase catalytic subunit alpha-2 (AMPKα2) is the kinase responsible for the phosphorylation of Ser272 in Bcl2-L-13.

RESULTS

Ablation of *Bcl2l13* led to reduced cardiac function after pressure overload

To investigate the *in vivo* role of Bcl2-L-13 in the heart, we generated Bcl2-L-13-deficient (*Bcl2l13*$^{-/-}$) mice. First, we designed a gene targeting strategy to conditionally inactivate the *Bcl2l13* gene by inserting *loxP* sites in introns 2 and 4 (Figure S1A). Homologous recombinants were identified using Southern blot analysis (Figure S1B). We then crossed homozygous floxed *Bcl2l13* mice (*Bcl2l13*$^{flox/flox}$) with transgenic mice expressing *Cre* recombinase under control of the β-actin promoter (*βActin-Cre* mice) to obtain conventional *Bcl2l13*$^{-/-}$ mice because global knockin mice were used in the following experiment. Mating between *Bcl2l13*$^{+/-}$ mice produced offspring with the expected Mendelian ratio (male *Bcl2l13*$^{+/+}$:male *Bcl2l13*$^{+/-}$:male *Bcl2l13*$^{-/-}$:female *Bcl2l13*$^{+/+}$:female *Bcl2l13*$^{+/-}$:female *Bcl2l13*$^{-/-}$ = 23:46:12:25:41:20). *Bcl2l13*$^{-/-}$ mice were viable, fertile, and normal in appearance. The efficiency of Bcl2-L-13 ablation in the heart was determined by immunoblot analysis. Bcl2-L-13 was totally abrogated in *Bcl2l13*$^{-/-}$ hearts (Figure S1C). There were no significant differences in physiological or echocardiographic parameters at 10 weeks of age between *Bcl2l13*$^{-/-}$ and *Bcl2l13*$^{+/+}$ mice (Table S1).

To examine the *in vivo* role of Bcl2-L-13 in the heart during cardiac stress, *Bcl2l13*$^{-/-}$ and *Bcl2l13*$^{+/+}$ mice were subjected to pressure overload via transverse aortic constriction (TAC) surgery. We used a 25G needle to exact mild pressure overload, which does not induce cardiac dysfunction and heart failure in *Bcl2l13*$^{+/+}$ mice but does induce cardiac hypertrophy. Four weeks after surgery, echocardiographic analysis revealed an increase in end-systolic left ventricular (LV) internal dimension (LVIDs) and a decrease in LV fractional shortening (FS), which is an index for systolic function, in the TAC-operated *Bcl2l13*$^{-/-}$ group, while the LV dimension and function of the TAC-operated *Bcl2l13*$^{+/+}$ group remained the same (Figures 1A and 1B). The thickness of the end-diastolic interventricular septum wall (IVSd) and LV posterior wall (LVPWd) was elevated in TAC-operated *Bcl2l13*$^{+/+}$ and *Bcl2l13*$^{-/-}$ mice compared to the corresponding sham-operated mice. The IVSd and LVPWd in TAC-operated *Bcl2l13*$^{-/-}$ mice were significantly shorter than in TAC-operated *Bcl2l13*$^{+/+}$ mice. The LV weight-to-tibia length ratio, an index for cardiac hypertrophy, was increased in TAC-operated groups compared to the corresponding sham groups; however, the extent of this increase was less in the TAC-operated *Bcl2l13*$^{-/-}$ group. There was no significant increase in lung-to-body weight ratio, an index for lung congestion, in either *Bcl2l13*$^{-/-}$ or *Bcl2l13*$^{+/+}$ mice (Figure 1C). The mRNA expression level of *Nppa*, which reflects cardiac hypertrophy, was increased in the TAC-operated *Bcl2l13*$^{+/+}$ and *Bcl2l13*$^{-/-}$ groups; however, levels were higher in the TAC-operated *Bcl2l13*$^{+/+}$ group. The mRNA expression level of *Nppb*, which primarily reflects LV dysfunction, was increased significantly in the TAC-operated *Bcl2l13*$^{-/-}$ group compared to all other groups (Figure 1D). Histological analysis revealed an increased fibrosis fraction in both TAC-operated groups; however, cellular infiltration was not observed in any group (Figures S1D and S1E). The cardiomyocyte cross-sectional area was larger in the TAC-operated *Bcl2l13*$^{+/+}$ group compared to the *Bcl2l13*$^{-/-}$ group (Figure 1E). These data suggest that ablation of *Bcl2l13* results in cardiac dysfunction with decreased hypertrophic responses against pressure overload.

Mitochondrial fission and mitophagy were attenuated in *Bcl2l13*$^{-/-}$ hearts after the TAC operation

To explore the molecular mechanisms underlying the abnormal cardiac phenotypes observed in *Bcl2l13*$^{-/-}$ mice, we analyzed the mice at the earlier time course after TAC. Cardiac function decreased in TAC-operated *Bcl2l13*$^{-/-}$ mice over time (Figure S2A). We chose to perform the analyses 5 days after TAC to minimize the contribution of operation-related events secondary to the initial and essential events that induced the cardiac phenotypes in *Bcl2l13*$^{-/-}$ mice. Five days after the operation, the TAC-operated *Bcl2l13*$^{-/-}$ hearts demonstrated LV systolic dysfunction, while the LV function of the TAC-operated *Bcl2l13*$^{+/+}$ group was maintained (Figure S2B). The IVSd, LVPWD, and LV weight-to-tibia length ratios were increased significantly to a similar extent in both TAC groups, and there was no significant increase in lung-to-body weight ratio (Figure S2C). In line with the echocardiographic and physiological analyses, the cardiomyocyte cross-sectional area was increased to a similar degree in both TAC groups (Figure S2D). In addition, we analyzed the contribution of cell death to the cardiac phenotypes. Apoptosis was detected by terminal transferase dUTP nick end labeling (TUNEL) staining, and necrosis was detected by the translocation of HMGB1 from the nucleus. Both apoptosis and necrosis were increased significantly by TAC operation, but there was no significant difference between TAC-operated *Bcl2l13*$^{+/+}$ and TAC-operated *Bcl2l13*$^{-/-}$ mice, suggesting that cell death is not involved in the cardiac dysfunction observed in *Bcl2l13*$^{-/-}$ mice (Figures S2E and S2F).

We have reported previously that Bcl2-L-13 induces both mitochondrial fission and mitophagy in mammalian cells.[8] In the current study, we examined whether Bcl2-L-13 performs these functions in *in vivo* hearts. First, we performed ultrastructural analysis. Using the Freehand selection tool, inter-myofibrillar mitochondria were traced. The mitochondrial long diameter, which is the primary axis of the best-fitting ellipse to the traced pixels, and the mitochondrial area were measured. The population of mitochondria with shorter long diameters or smaller areas was increased significantly after TAC in *Bcl2l13*$^{+/+}$ mice, whereas it was significantly decreased in *Bcl2l13*$^{-/-}$ mice (Figures 2A–2C and S3A). In addition, we evaluated the protein levels of peroxisome proliferator-activated receptor gamma coactivator 1-alpha (PGC1α) to examine the contribution of mitochondrial biogenesis to mitochondrial morphological changes (Figure S3B). The protein levels of PGC1α were similar in all groups. These data suggest that pressure overload-induced mitochondrial fission was attenuated in *Bcl2l13*$^{-/-}$ hearts. We subsequently analyzed protein levels to examine the involvement of the molecules related to mitochondrial fusion and fission in this phenotype (Figures S3C and S3D). Dynamin-related protein 1 (Drp1) induces mitochondrial

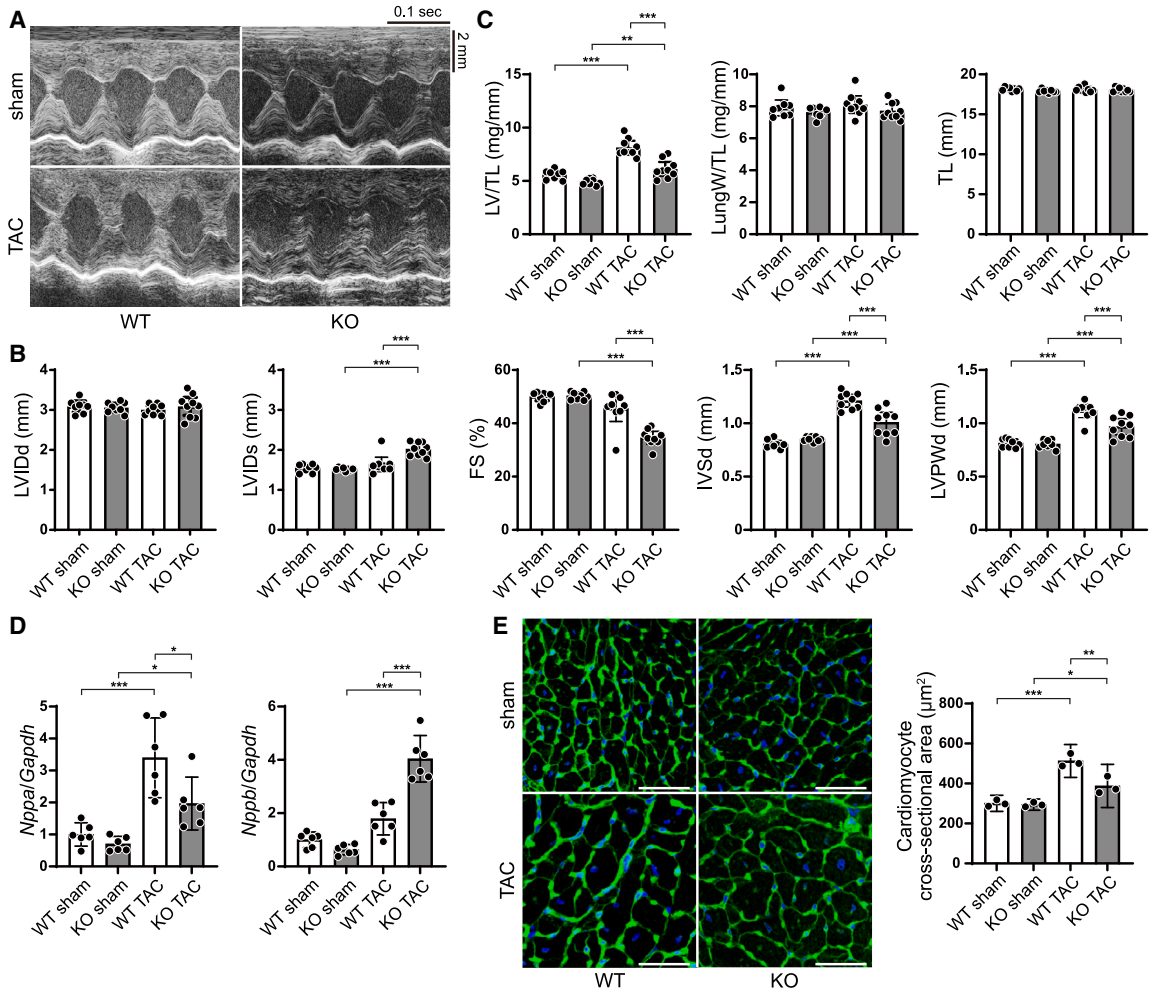

Figure 1. Pressure overload-induced cardiac dysfunction in *Bcl2l13*$^{-/-}$ mice

Bcl2l13$^{+/+}$ (WT) and *Bcl2l13*$^{-/-}$ (KO) mice were subjected to pressure overload by means of transverse aortic constriction (TAC). The mice were analyzed 4 weeks after TAC.

(A) Representative images of M-mode echocardiographic tracings from sham- or TAC-operated WT or KO mice. Scale bars: 0.1 s and 2 mm.

(B) Echocardiographic parameters. n = 8 (WT sham), 8 (KO sham), 9 (WT TAC), or 9 (KO TAC) per group. LVIDd, end-diastolic left ventricular internal dimension; LVIDs, end-systolic left ventricular internal dimension; FS, fractional shortening; IVSd, end-diastolic interventricular septum wall thickness; LVPWd, end-diastolic left ventricular posterior wall thickness.

(C) Physiological parameters. n = 8 (WT sham), 8 (KO sham), 9 (WT TAC), or 9 (KO TAC) per group. LV/TL, left ventricular weight/tibia length; lungW/TL, lung weight/tibia length.

(D) mRNA expression of *Nppa* and *Nppb* (n = 6). *Gapdh* mRNA was used as the loading control. The average value in the WT sham group was set to 1.

(E) Wheat germ agglutinin-stained heart sections. Scale bar: 50 μm. Cardiomyocyte cross-sectional areas were measured by tracing the outline of 100 myocytes in the non-fibrotic area on each section (n = 3). Results are shown as mean with 95% confidence intervals (CIs). Statistical analysis included one-way ANOVA followed by Tukey-Kramer's post hoc test. All pairwise comparisons were performed. *p < 0.05, **p < 0.01, ***p < 0.001. See also Figure S1.

fission by interacting with fission-related protein 1.[14] Phosphorylation of Drp1 at Ser616 promotes mitochondrial fission, while phosphorylation of Drp1 at Ser637 inhibits mitochondrial fission.[15,16] In contrast, mitofusin 1 (Mfn1) and Mfn2 and optic atrophy 1 increase the formation of elongated mitochondrion networks. The protein level of phosphorylated Drp1 (Ser616) was upregulated significantly in TAC-operated *Bcl2l13*$^{-/-}$ mice compared to the sham-operated control; however, this can be considered a compensatory change. The expression of other proteins did not show significant differences among groups.

Mitophagy was evaluated using immunohistochemical analysis, whereby mitophagy was identified by colocalizing the autophagosome marker LC3B and mitochondrion marker ATP synthase. Five days after TAC, mitophagy was upregulated significantly in *Bcl2l13*$^{+/+}$ hearts, while there was no significant difference between sham-operated and TAC-operated *Bcl2l13*$^{-/-}$ hearts (knockout [KO] sham vs. KO TAC: p = 0.8446; relative values for each group to WT sham group: KO sham group 0.476, wild-type [WT] TAC group 2.31, KO TAC group 0.636) (Figure 2D).

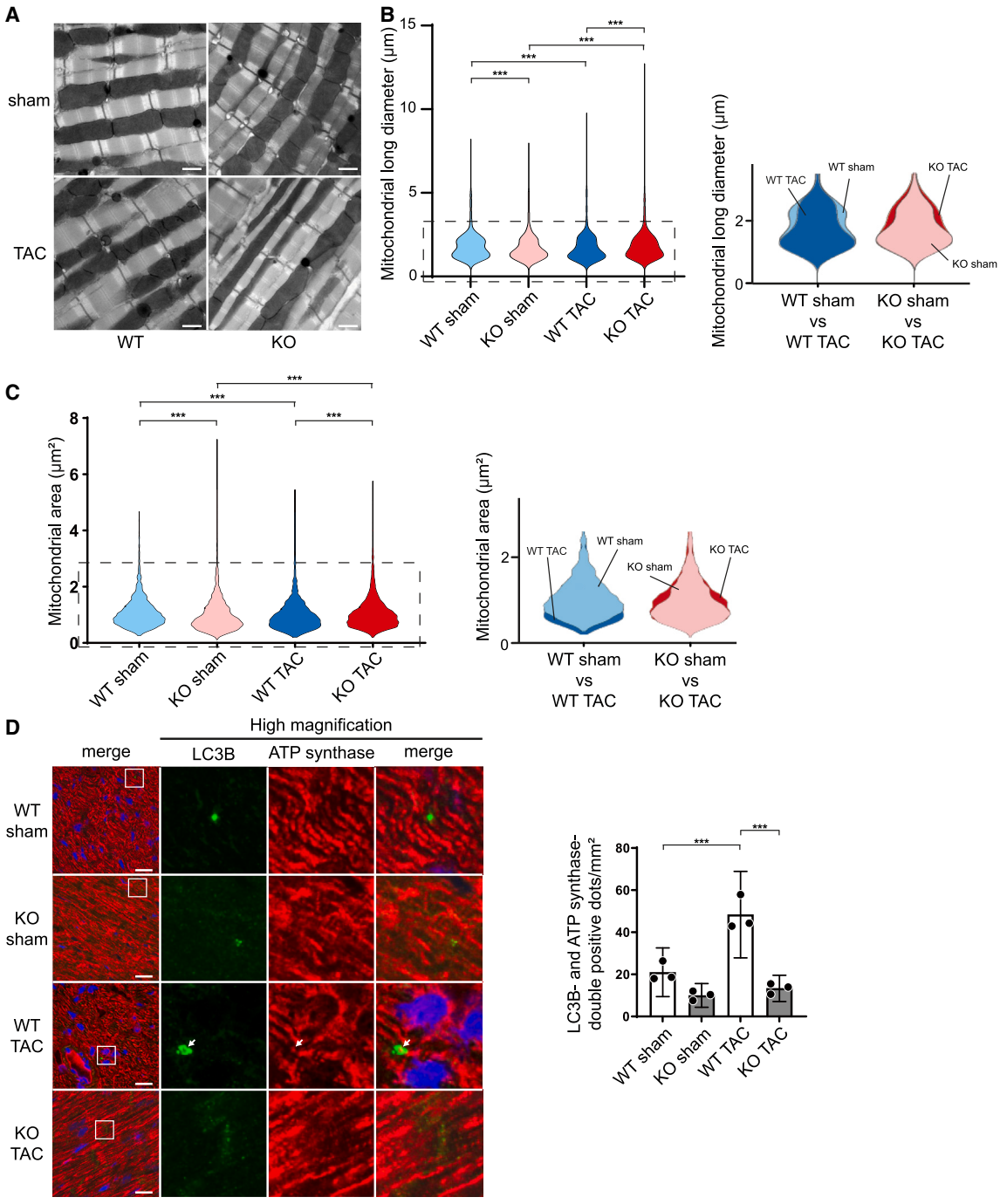

Figure 2. Mitochondrial morphology and mitophagy in TAC-operated *Bcl2l13*$^{-/-}$ mice

(A) Electron micrographs of mouse hearts 5 days after TAC. Scale bar: 1 μm.

(B and C) Violin plots visualizing the distribution of long diameters and areas of mitochondria measured in (A). Using the Freehand selection tool, inter-myofibrillar mitochondria were traced. The long diameter is the primary axis of the best-fitting ellipse to the traced pixels. The area enclosed by the dotted line in the violin plots is enlarged and shown on the right, with two groups overlaid. The histogram of the distribution of long diameters is shown in Figure S3A.

(D) Immunostaining of LC3B and ATP synthase in the heart 5 days after TAC. Scale bar: 20 μm. Images in the box at higher magnification are shown on the right. The white arrow indicates the colocalization of LC3B and ATP synthase double-positive dot. The number of LC3B and ATP synthase double-positive dots per 1 mm^2 is shown in the bar graph (n = 3). Results are shown as mean with 95% CI. Statistical analysis by Kruskal-Wallis test in (B) and (C) and one-way ANOVA followed by Tukey-Kramer's post hoc test in (D). All pairwise comparisons were performed. ***$p < 0.001$. See also Figures S2 and S3.

Parkin has been reported to be upregulated due to cardiac pressure overload.[17,18] Therefore, we examined the involvement of Parkin in cardiac dysfunction in TAC-operated *Bcl2l13*$^{-/-}$ hearts. In agreement with previous findings, the protein level of Parkin was upregulated in both TAC groups; however, there was no significant difference between TAC-operated *Bcl2l13*$^{+/+}$ and *Bcl2l13*$^{-/-}$ mice (Figure S3E). Furthermore, there were no significant differences in PINK1 expression between the groups. To examine the contribution of Parkin-dependent mitophagy to the cardiomyopathy seen in TAC-operated *Bcl2l13*$^{-/-}$ mice, we generated double KO mice of Bcl2-L-13 and Parkin. If Parkin has a pivotal role in maintaining cardiac function under pressure overload independent of Bcl2-L-13, then *Bcl2l13*$^{-/-}$*Prk2*$^{-/-}$ mice would show worse cardiac function than *Bcl2l13*$^{-/-}$*Prk2*$^{+/+}$ mice. TAC-operated *Bcl2l13*$^{-/-}$*Prk2*$^{-/-}$ mice showed a similar level of cardiac dysfunction as *Bcl2l13*$^{-/-}$*Prk2*$^{+/+}$ mice, suggesting that Parkin does not play a pivotal role in cardiac reaction against pressure overload in *Bcl2l13*$^{-/-}$ mice (Figures S3F and S3G).

Mitochondrial reactive oxygen species production was increased and ATP production was reduced in TAC-operated *Bcl2l13*$^{-/-}$ hearts

Downregulation of mitophagy might result in attenuation of the removal of dysfunctional mitochondria, leading to increased reactive oxygen species (ROS) production and reduced ATP production in cardiomyocytes. We isolated cardiomyocytes 5 days after TAC and evaluated ROS using the mitochondrial superoxide indicator MitoSOX (Figure 3A). We identified mitochondria strongly stained with MitoSOX only in cardiomyocytes isolated from TAC-operated *Bcl2l13*$^{-/-}$ mice. Furthermore, we analyzed mitochondrial DNA (mtDNA) damage by evaluating the level of replicated 8.2 kb mtDNA using a mouse real-time PCR mitochondrial DNA damage analysis kit. The damage to the mtDNA results in the inhibition of PCR of 8.2 kb mtDNA. In agreement with the results from the MitoSOX analysis, the amount of 8.2 kb-PCR product was decreased significantly in TAC-operated *Bcl2l13*$^{-/-}$ hearts, indicating increased mtDNA damage (Figure S3H). Next, we evaluated the mitochondrial respiration of isolated cardiomyocytes 5 days after TAC using a Seahorse XFe24 extracellular flux analyzer (Figure 3B). The mitochondrial stress test demonstrated that the baseline oxygen consumption rate (OCR) of *Bcl2l13*$^{+/+}$ cardiomyocytes was upregulated significantly in response to pressure overload, while it was unchanged in *Bcl2l13*$^{-/-}$ mice. Furthermore, maximum OCR and ATP concentration were decreased significantly in TAC-operated *Bcl2l13*$^{-/-}$ hearts (Figures 3B and 3C). These data suggest that damaged mitochondria escaped from mitophagic degradation produced more ROS and less ATP and were accumulated in TAC-operated *Bcl2l13*$^{-/-}$ hearts.

A phosphorylation-silencing mutation of Bcl2-L-13 led to reduced cardiac function in response to pressure overload

We have shown previously that the phosphorylation of Bcl2-L-13 at Ser272 is important for the mitophagic activity of Bcl2-L-13.[8] To evaluate the level of phosphorylation, we generated an antibody against phospho-Bcl2-L-13 (Ser272). The antibody recognized a band in the lysate isolated from HEK293 cells expressing WT Bcl2-L-13, whereas it recognized a weak signal from the lysates of cells expressing Bcl2-L-13 (S272A) (Figure S4A). In *Bcl2l13*$^{+/+}$ mice, the phosphorylation level of Bcl2-L-13 at Ser272 increased 4 weeks after the TAC operation, suggesting that the phosphorylation of Bcl2-L-13 was upregulated in response to pressure overload (Figure 4A). To investigate the *in vivo* role of the phosphorylation of Bcl2-L-13 at Ser272 in the heart, we generated knockin mice (*Bcl2l13*$^{S272A/S272A}$), in which the phosphorylation site (Ser272) on Bcl2-L-13 was changed to Ala (Figure S4B). *Bcl2l13*$^{WT/S272A}$ mice were crossed to obtain *Bcl2l13*$^{S272A/S272A}$ mice. Mice were born at the expected Mendelian ratios (male *Bcl2l13*$^{w/w}$:male *Bcl2l13*$^{WT/S272A}$:male *Bcl2l13*$^{S272A/S272A}$:female *Bcl2l13*$^{w/w}$:female *Bcl2l13*$^{WT/S272A}$:female *Bcl2l13*$^{S272A/S272A}$ = 14:36:9:11:27:12). *Bcl2l13*$^{S272A/S272A}$ mice showed similar physiological parameters and cardiac function compared to WT mice (Table S2). A western blot analysis indicated that the protein level of phospho-Bcl2-L-13 (Ser272) was reduced significantly in *Bcl2l13*$^{S272A/S272A}$ (Figure S4C).

We subsequently subjected those mice to pressure overload using a 25G needle. The *Bcl2l13*$^{S272A/S272A}$ mice exhibited LV chamber dilation and cardiac dysfunction 4 weeks after surgery, while the LV function of the TAC-operated *Bcl2l13*$^{w/w}$ group was maintained (Figures 4B and 4C). Although TAC increased the LV weight-to-tibia length ratio in both groups, this ratio was significantly higher in *Bcl2l13*$^{S272A/S272A}$ mice (Figure 4D). There was no significant increase in lung-to-body weight ratio in either TAC group. The mRNA levels of *Nppa* and *Nppb* were significantly higher in TAC-operated *Bcl2L13*$^{S272A/S272A}$ hearts compared to all other groups (Figure 4E). From histological analysis, cellular infiltration was not observed in any group (Figure S4D). The fibrosis fraction (Figure S4E) and cardiomyocyte cross-sectional area (Figure 4F) were increased in both TAC-operated groups. TAC-operated *Bcl2l13*$^{S272A/S272A}$ hearts demonstrated larger fibrosis fractions and cross-sectional areas than TAC-operated WT mice. These data suggest that the phosphorylation of Bcl2-L-13 at Ser272 plays an important role in maintaining cardiac function under pressure overload.

We examined mitochondrial morphology and mitophagic activity 5 days after TAC. As the Bcl2-L-13 (S272A) mutant maintained its ability to induce mitochondrial fission in the *in vitro* study,[8] we expected TAC-operated *Bcl2l13*$^{S272A/S272A}$ mice to display a mitochondrial morphology similar to TAC-operated *Bcl2l13*$^{w/w}$. However, contrary to our expectations, the population of mitochondria with longer lengths and smaller mitochondrial areas was increased in TAC-operated *Bcl2l13*$^{S272A/S272A}$ mice (Figures 5A–5C and S5A). Fusion/fission-related molecules showed no differences in protein or phosphorylation levels between TAC-operated groups (Figures S5B and S5C). Immunohistochemical analysis revealed that TAC-operated *Bcl2l13*$^{S272A/S272A}$ mice had significantly lower levels of mitophagy than TAC-operated *Bcl2l13*$^{w/w}$ mice (Figure 5D). Furthermore, the cytosolic ATP concentration in TAC-operated *Bcl2l13*$^{S272A/S272A}$ hearts was lower than in *Bcl2l13*$^{w/w}$ hearts (Figure 5E). While the protein level of Parkin was upregulated in both TAC groups, there was no significant difference in the level between TAC-operated WT and knockin mice (Figure S5D). In addition, there were no significant differences in PINK1

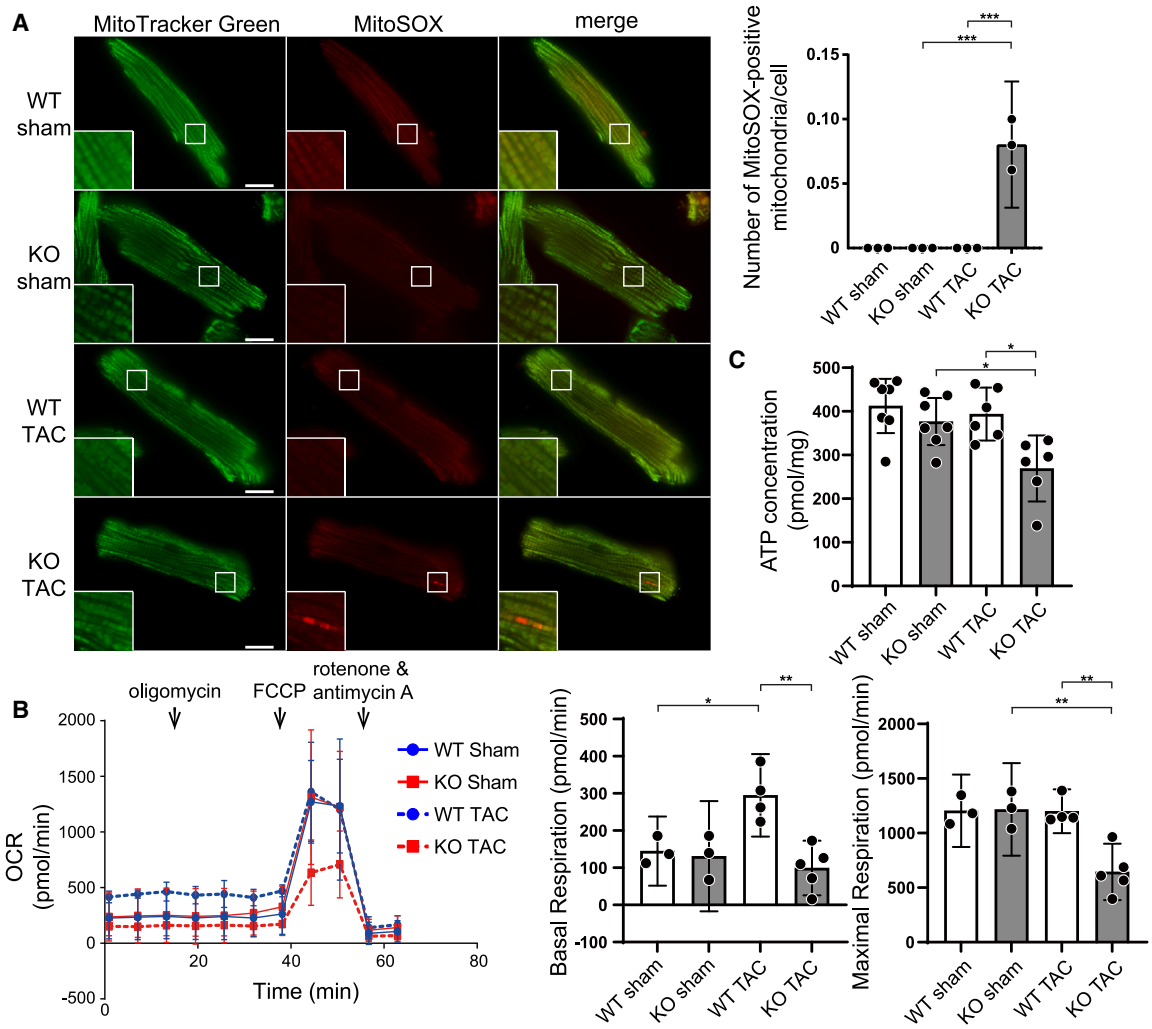

Figure 3. Mitochondrial dysfunction in TAC-operated *Bcl2l13*$^{-/-}$ mice

(A) Mitochondrial reactive oxygen species (ROS) production in cardiomyocytes. Cardiomyocytes were isolated 5 days after the TAC operation and stained with MitoSOX and MitoTracker Green for confocal microscopy ($n = 3$). MitoSOX-positive mitochondria in the boxed area are shown at higher magnification in the inset. Scale bar: 10 μm. The number of MitoSOX-positive mitochondria per cell is shown in the bar graph. At least 30 cells were observed in each experiment.

(B) The oxygen consumption rate (OCR) of isolated cardiomyocytes 5 days after TAC was assessed using the Seahorse XF24 extracellular flux analyzer. $n = 3$ (WT sham), 3 (KO sham), 3 (WT TAC), or 5 (KO TAC) per group. Reagents were injected sequentially during the assay to yield final concentrations of 1 μM oligomycin, 2 μM carbonyl cyanide 4-(trifluoromethoxy) phenylhydrazone (FCCP), 2 μM rotenone, and 4 μM antimycin A. Basal respiration and maximal respiration are shown in the bar graphs.

(C) Tissue ATP levels were measured using the left ventricle from mice 5 days after TAC. $n = 7$ (WT sham), 7 (KO sham), 6 (WT TAC), or 6 (KO TAC) per group. Results are shown as mean with 95% CI. Statistical analysis by one-way ANOVA followed by Tukey-Kramer's post hoc test. All pairwise comparisons were performed. *$p < 0.05$, **$p < 0.01$, ***$p < 0.001$.

expression between the groups. Therefore, *Bcl2l13* ablation and the S272A mutation had detrimental effects on the cardiac phenotype and comparable impacts on the mitochondria dynamics in response to pressure overload.

Kinase siRNA library screening revealed that AMPKα2 is the kinase responsible for Bcl2-L-13 phosphorylation at Ser272

To further explore the mechanism of Bcl2-L-13 activation, we attempted to determine the kinase responsible for the phosphorylation of Bcl2-L-13 at Ser272. To establish an assay suitable for manual screening using the small interfering RNA (siRNA) library of kinases, we tested whether phospho-Bcl2-L-13 is detectable by fluorescence immunocytochemistry using HEK293 cells that stably expressed HA-Bcl2-L-13. Carbonyl cyanide *m*-chlorophenylhydrazone (CCCP), a mitochondrial oxidative phosphorylation uncoupler, induces mitophagy. Phospho-Bcl2-L-13-positive dots were detected after administration of bafilomycin A1 and CCCP, and they were colocalized with signals from the anti-hemagglutinin (HA) antibody (Figure S6A). To confirm the colocalization between HA and phospho-Bcl2-L-13, we performed quantification analysis using the JACoP plugin of ImageJ

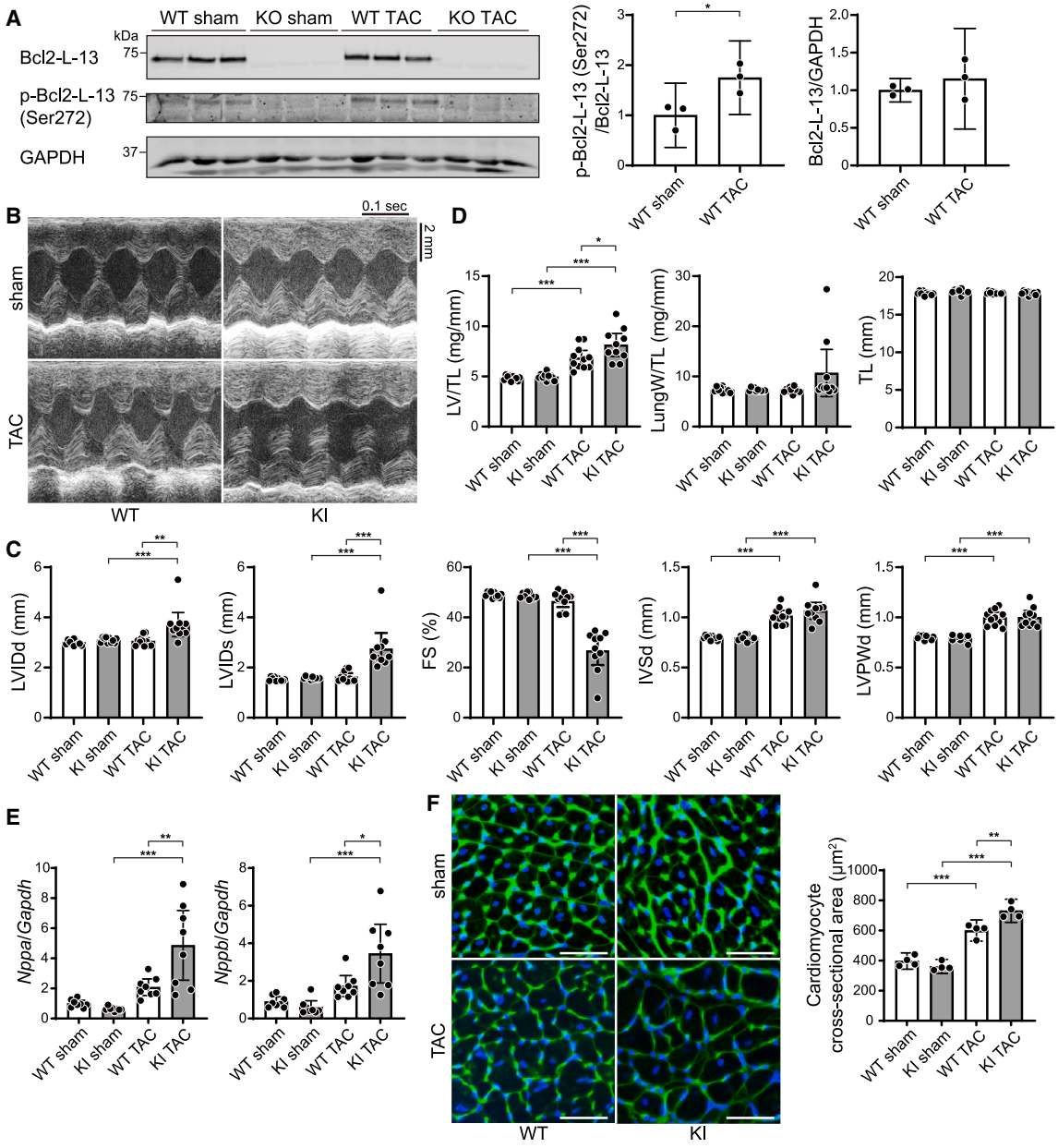

Figure 4. Pressure overload-induced cardiac dysfunction in Bcl2-L-13 (S272A) knockin mice

(A) Western blot analysis of phospho- Bcl2-L-13 (Ser272) in the *Bcl2l13*$^{+/+}$ (WT) and *Bcl2l13*$^{-/-}$ (KO) mouse hearts 4 weeks after TAC ($n = 3$). The bar graph shows densitometric analysis.

(B) Representative images of M-mode echocardiographic tracings from sham- or TAC-operated wild-type (WT) or Bcl2-L-13 (S272A) knockin (KI) mice 4 weeks after surgery. Scale bars, 0.1 s and 2 mm.

(C) Echocardiographic parameters ($n = 10$).

(D) Physiological parameters ($n = 10$).

(E) mRNA expression of *Nppa* and *Nppb* ($n = 8$). *Gapdh* mRNA was used as the loading control. The average value in the WT sham group was set to 1.

(F) Wheat germ agglutinin-stained heart sections. Scale bar: 50 μm. Cardiomyocyte cross-sectional areas were measured by tracing the outline of 100 myocytes in a non-fibrotic area in each section ($n = 4$). Results are shown as mean with 95% CI. Statistical analysis by one-way ANOVA followed by Tukey-Kramer's post hoc test. All pairwise comparisons were performed. *$p < 0.05$, **$p < 0.01$, ***$p < 0.001$. See also Figure S4.

to obtain the Manders' coefficients of the images presented in Figure S6A[19,20] The results showed that, in DMSO-treated cells, the Manders' coefficient was 0.938, while that in CCCP-treated cells was 0.967. These results strongly suggest that the green signals from the HA antibody colocalize with the red signals from the phospho-Bcl2-L-13 antibody. A primary screen using the Silencer Human Kinase siRNA Library (708 genes, three siRNAs per gene) was carried out (Figures 6A and S6B). For

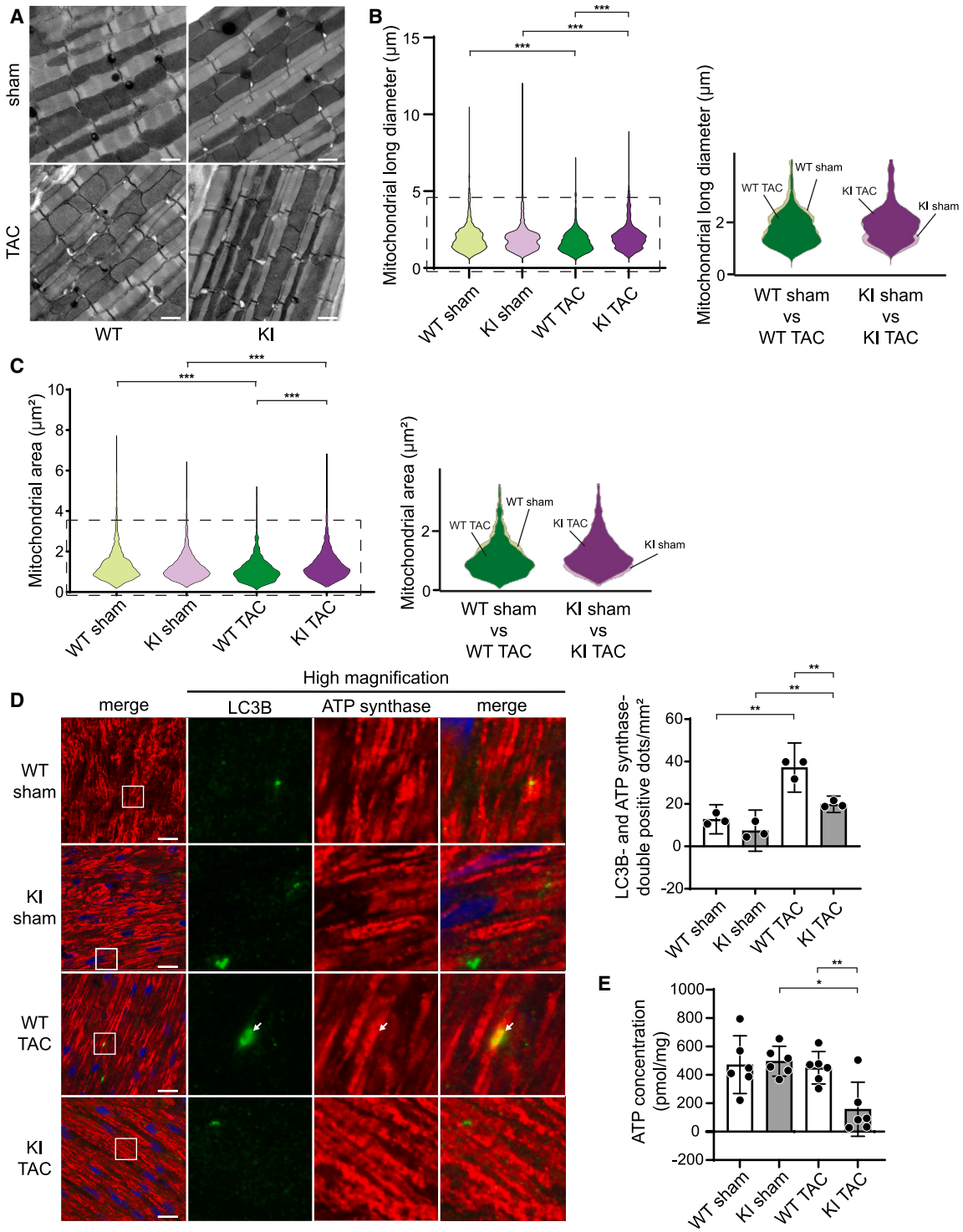

Figure 5. Mitochondrial morphology, mitophagy, and ATP concentration in TAC-operated Bcl2-L-13 (S272A) KI hearts

(A) Electron micrographs of mouse hearts 5 days after TAC. Scale bar: 1 μm.

(B and C) Violin plots visualizing the distribution of long diameters and areas of mitochondria measured in (A). Using the Freehand selection tool, inter-myofibrillar mitochondria were traced. The long diameter is the primary axis of the best-fitting ellipse to the traced pixels. The area enclosed by the dotted line in the violin plots is enlarged and shown on the right, with two groups overlaid. The histogram of the distribution of long diameters is shown in Figure S5A.

(legend continued on next page)

quantification of phospho-Bcl2-L-13 (Ser272)-positive dots, local maxima were determined using the "find maxima" function of ImageJ. Candidates that were able to reduce the number of phospho-Bcl2-L-13 (Ser272)-positive dots induced by CCCP treatment were selected. The criteria for selection, which were determined in the preliminary experiments, were an over 60% reduction in phospho-Bcl2-L-13 (Ser272)-positive dots compared with positive controls in at least one of three siRNAs or an over 40% reduction in at least two siRNAs. From this, a collection of 74 genes were identified (Table S3). Furthermore, *Z* scoring was used to confirm our screening criteria. We obtained 64 genes with a *Z* score greater than 1.5 as hits. All of them were included in the identified 74 genes (Figure S6C; Table S6).

To narrow down the candidates, we conducted a secondary screen (Figure S6D). As the knockdown of the responsible kinase should reduce Bcl2-L-13-mediated mitophagy, we evaluated mitophagy induced by CCCP via fluorescence immunocytochemistry using anti-ATP synthase and anti-LC3B antibodies after knockdown of the candidate genes. Mitophagy was evaluated manually by counting the number of ATP synthase dots colocalized with LC3B dots. At least 20 cells were quantified. We carried forward 18 genes that demonstrated a more than 40% reduction of ATP synthase- and LC3B-colocalized dots compared with the positive control (Table S4). The criteria for selection were determined in the preliminary experiment. We also evaluated mitophagy using the JACoP plugin of ImageJ for colocalization analysis.[19,20] We identified 9 genes with a *Z* score greater than 1.0 as hits (Figure S6E; Tables S4 and S6). As seven candidates obtained from counting with software overlapped with those from manual counting, we carried forward 20 genes in total. Since the phosphorylation target is a serine residue, we selected 14 genes that have been reported to have serine/threonine-protein kinase activity. We tested the kinase activity of these 14 candidates by *in vitro* kinase assay. For this assay, purified candidate kinases were mixed with bacterially synthesized HA-Bcl2-L-13 and 1 mM ATP. The reaction mix was subjected to western blot analysis. Of 14 candidates, AMPKα2 was found to significantly upregulate the phospho-Bcl2-L-13 protein level (Figure 6B). Synthesized HA-Bcl2-L-13 (S272A) was not phosphorylated by purified AMPKα2 protein (Figure S6F).

To validate the screening results, we evaluated Bcl2-L-13 phosphorylation in AMPKα2 knockdown cells. The protein level of phospho-Bcl2-L-13 increased 1 h after CCCP administration (Figure 6C). While knockdown of AMPKα2 significantly reduced the phosphorylation level of Bcl2-L-13, knockdown of the isoform of AMPKα, AMPKα1, did not (Figures 6C and S6G). To confirm the upregulation of AMPKα2 activity by CCCP, we induced knockdown of AMPKα1 and measured AMPKα activity (Figure 6D). CCCP significantly upregulated AMPKα2 activity for 1 h. We tested the effect of a known AMPK inhibitor, compound C, and an AMPK activator, quercetin, on CCCP-induced phosphorylation of Bcl2-L-13. Compound C significantly reduced the protein level of phospho-Bcl2-L-13, while quercetin significantly upregulated it (Figures S7A and S7B). To explore upstream stimuli to activate AMPKα2 other than decreased ATP level, we assessed the effect of a ROS inhibitor, N-acetyl-L-cysteine (NAC), and a calcium chelator, *O*,*O*'-Bis(2-aminophenyl)ethyleneglycol-*N*,*N*,*N*',*N*'-tetraacetic acid, tetraacetoxymethyl ester (BAPTA-AM), on CCCP-induced phosphorylation of Bcl2-L-13 (Figures S7C and S7D). NAC had no effect on the phosphorylation of Bcl2-L-13, while BAPTA-AM inhibited CCCP-induced phosphorylation. Because calcium/calmodulin-dependent protein kinase kinase 2 (CaMKK2) is an upstream kinase of AMPK, and its activity depends on intracellular calcium concentration, we conducted a knockdown experiment (Figure S7E). Knockdown of CaMKK2 significantly reduced the phosphorylation level of Bcl2-L-13, suggesting that intracellular calcium signaling through CaMKK2 is important for Bcl2-L-13 phosphorylation. Next, we evaluated Bcl2-L-13-induced mitophagy using the JACoP plugin of ImageJ for colocalization analysis.[19,20] As we reported previously, overexpression of Bcl2-L-13 increased mitophagy (Figures 6E and 6F). Knockdown of AMPKα2 significantly reduced ATP synthase and LC3B double-positive dots. Finally, we evaluated the activity of AMPKα2 and AMPKα2-Bcl2-L-13 interaction in TAC-operated hearts. To quantify AMPKα2-specific phosphorylation, we immunoprecipitated AMPKα2 and immunoblotted with an anti-phospho-AMPKα Thr172 antibody (Figure 6G). The phosphorylation of AMPKα2 was increased significantly in TAC-operated *Bcl2l13*$^{+/+}$ mice, while phosphorylation of AMPKα2 was suppressed in *Bcl2l13*$^{-/-}$ hearts 5 days after TAC. To investigate whether Bcl2-L-13 forms a complex with AMPKα2 in the heart after TAC, an immunoprecipitation experiment was conducted (Figure 6H). AMPKα2 precipitated Bcl2-L-13, and the interaction was upregulated significantly following TAC operation. We concluded that AMPKα2 is the kinase responsible for phosphorylating Ser272 on Bcl2-L-13.

DISCUSSION

Our data indicate that Bcl2-L-13 is not required for normal embryonic development. Because the heart is one of the organs that shows the highest mRNA expression levels of Bcl2-L-13, we primarily analyzed the heart in this study. We demonstrated that Bcl2-L-13-deficient mice showed normal cardiac structure and function under basal conditions, indicating that Bcl2-L-13 is not essential for the development or postnatal growth of the heart. In stressed hearts, Bcl2-L-13 plays a protective role in the development of cardiac dysfunction induced by pressure overload.

(D) Immunostaining of LC3B and ATP synthase in the heart 5 days after TAC. Scale bar: 20 μm. Images in the box at higher magnification are shown on the right. The white arrows indicates the colocalization of LC3B and ATP synthase double-positive dots. The number of LC3B and ATP synthase double-positive dots per 1 mm^2 is shown in the bar graph (n = 3).

(E) Tissue ATP levels measured using the left ventricle from mice 5 days after TAC (n = 6). Results are shown as mean with 95% CI. Statistical analysis by Kruskal-Wallis test in (B) and (C) and one-way ANOVA followed by Tukey-Kramer's post hoc test in (D) and (E). All pairwise comparisons were performed. *p < 0.05, **p < 0.01, ***p < 0.001. See also Figure S5.

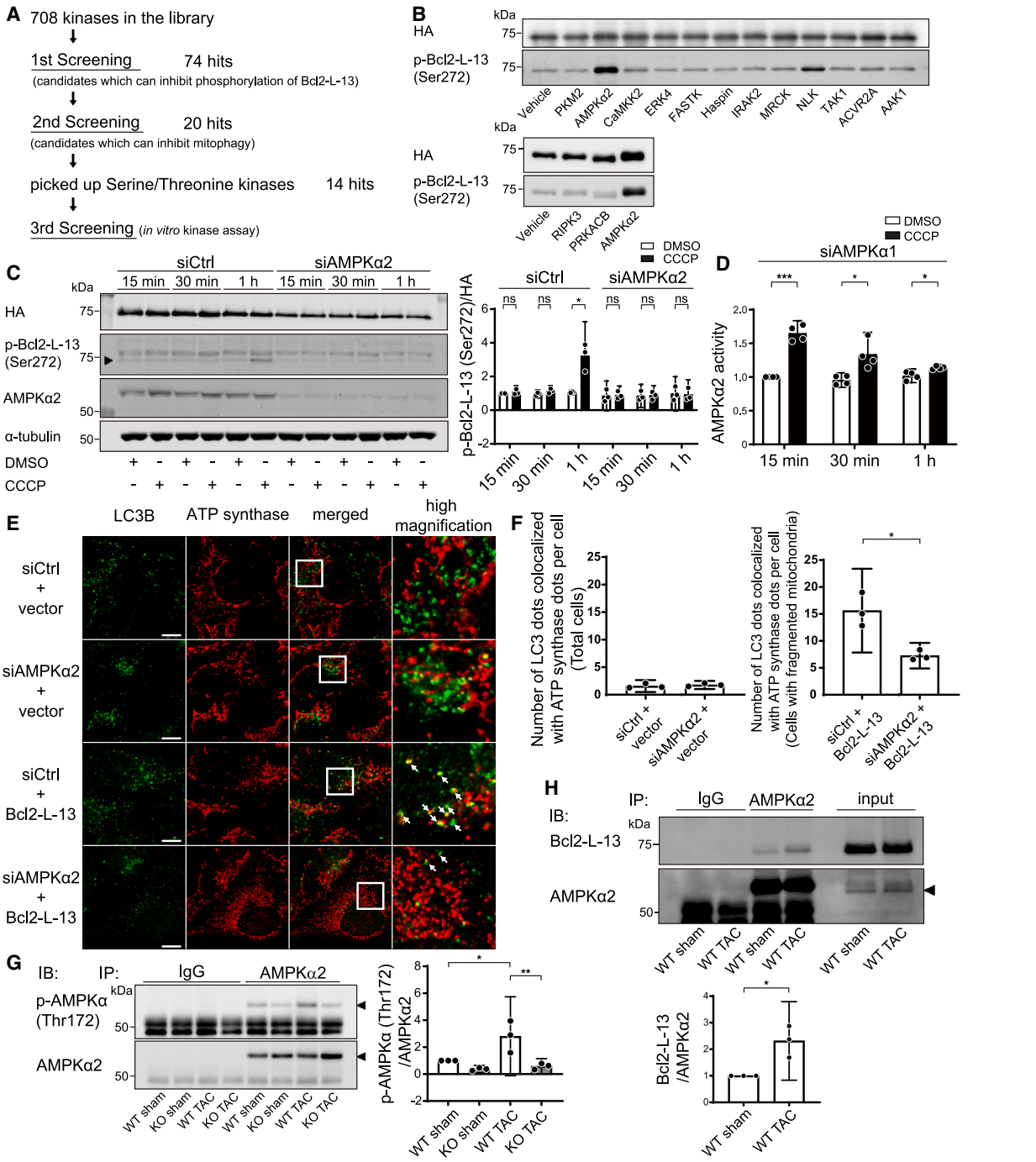

Figure 6. AMPKα2 is the kinase responsible for Bcl2-L-13 phosphorylation at Ser272

(A) Schematic of the responsible kinase screening workflow.

(B) *In vitro* kinase assay in the third screening. Bacterially synthesized HA-Bcl2-L-13 was mixed with purified candidate proteins and ATP. After incubation at 37°C for 30 min, the reaction mix was subjected to western blotting using an anti-phospho-Bcl2-L-13 (Ser272) antibody.

(C) The effect of AMPKα2 knockdown in CCCP-induced Bcl2-L-13 phosphorylation. HEK293A cells stably expressing HA-Bcl2-L-13 were transfected with control siRNA or siAMPKα2 for 72 h. Then, the cells were treated with DMSO or 15 μM CCCP for the indicated times, and cell lysates were subjected to western blot analysis. Densitometric analysis of phospho-Bcl2-L-13 (Ser272) is shown in the bar graph. The value for the group with control siRNA (siCtrl) transfection and 15 min of DMSO treatment in each experiment was set to 1 (n = 3).

(D) Upregulation of AMPKα2 activity by CCCP treatment. To analyze AMPKα2-specific activity, HEK293A cells stably expressing HA-Bcl2-L-13 were transfected with siAMPKα1 for 72 h and then treated with DMSO or 15 μM CCCP. The value for the group with 15-min DMSO treatment in each experiment was set to 1 (n = 4).

(legend continued on next page)

In our previous study, we hypothesized that a mammalian mitophagy receptor would share certain molecular features with Atg32, which is essential for mitophagy in yeast, and identified Bcl2-L-13 as a functional homolog of Atg32.[8] Bcl2-L-13 mediates mitochondrial fission and mitophagy in HEK293 cells. The interaction between Bcl2-L-13 and LC3B is required for Bcl2-L-13-mediated mitophagy, suggesting that Bcl2-L-13 is involved in the canonical mitophagy pathway. From *in vivo* analysis, our data showed that ablation of *Bcl2l13* decreased mitochondrial fission and mitophagy induced by TAC operation in the heart. Parkin is a well-characterized molecule related to the regulation of mitophagy and has been reported to have a protective or detrimental role under pressure overload in the heart.[17,18] We examined its involvement in the cardiac dysfunction observed in TAC-operated *Bcl2l13*$^{-/-}$ mice. However, ablation of Parkin did not demonstrate additional effects on cardiac function after TAC operation, suggesting that Parkin is dispensable for maintaining cardiac function in TAC-operated *Bcl2l13*$^{-/-}$ hearts. Then, we analyzed mitochondrial respiration and ATP levels. In agreement with previous reports, oligomycin addition did not decrease the OCR in adult mouse cardiomyocytes in this study.[21–23] This may be explained by decreased ATP demand of noncontracting adult cardiomyocytes and a relatively high rate of proton leak. *Bcl2l13*$^{-/-}$ hearts could not upregulate basal mitochondrial respiration in response to pressure overload and produced significantly less ATP than *Bcl2l13*$^{+/+}$ hearts. These results suggest that attenuation of mitochondrial fission and mitophagy by *Bcl2l13* ablation leads to the accumulation of damaged mitochondria, which produce less ATP, ultimately resulting in cardiac dysfunction.

Receptor-mediated mitophagy depends on the phosphorylation of mitochondrial outer membrane-anchored receptors, such as NIX, BNIP3, and FUNDC1. NIX and BNIP3 have been reported to be phosphorylated at Ser34 or Ser17 and Ser24 flanking the LC3-interacting region (LIR), respectively,[11,24] while FUNDC1 is phosphorylated at Tyr18, Ser13, and Ser17.[10–12] We have reported previously that the phosphorylation of Ser272 on Bcl2-L-13, flanking the LIR, is essential for the mitophagic activity of Bcl2-L-13 in HEK293 cells. In this study, our data showed that the protein level of phospho-Bcl2-L-13 (Ser272) was upregulated in response to pressure overload. To investigate the importance of Bcl2-L-13 phosphorylation in pressure-overloaded hearts, we generated Bcl2-L-13 phosphorylation site-deficient knockin mice. The knockin mice demonstrated cardiac dysfunction 4 weeks post-TAC, suggesting that the activation of Bcl2-L-13 by phosphorylation is vital for maintaining cardiac function.

While the kinases responsible for BNIP3 and NIX activation remain unknown, FUNDC1 has been reported to be phosphorylated by Src kinase, casein kinase 2, and ULK1. In this study, we attempted to identify a kinase responsible for Ser272 phosphorylation on Bcl2-L-13. A series of screenings using siRNA or *in vitro* kinase assays identified AMPKα2 as the responsible kinase. The *in vitro* kinase assay and co-immunoprecipitation studies from endogenous proteins demonstrated that AMPKα2 binds to Bcl2-L-13 in the stressed heart and directly phosphorylates Bcl2-L-13. Previous studies have reported that AMPK regulates mitophagy through the phosphorylation of ULK1.[25] Furthermore, we previously identified a mechanism of Bcl2-L-13-mediated mitophagy induction whereby Bcl2-L-13 recruits the ULK1 complex to recruit mitophagy machinery.[26] Myristoylation of the β subunit of AMPK has been shown to localize AMPK to mitochondria during mitophagy.[27] Thus, AMPK activates ULK1 to initiate autophagosome formation and migrates to mitochondria to directly phosphorylate Bcl2-L-13 for mitophagy induction. Therefore, we propose a model where pressure overload damages mitochondria, leading to a decrease in ATP production, which activates AMPK. AMPK subsequently phosphorylates Bcl2-L-13 to activate mitophagy for the degradation of damaged mitochondria, which may produce detrimental ROS (Figure 7). Moreover, our *in vivo* analysis revealed that the phosphorylation of AMPKα2 was upregulated significantly by pressure overload. Unexpectedly, the phosphorylation was attenuated in *Bcl2l13*$^{-/-}$ hearts. This suggests that Bcl2-L-13 itself might be involved in AMPKα2 activation in the stressed heart.

AMPK is a heterotrimeric complex comprising a catalytic α subunit and two regulatory subunits, β and γ. The two α subunits, α1, and α2, are encoded by the discrete genes *PRKAA1* and *PRKAA2*. Although the α1 and α2 isoforms are 90% identical within the kinase domains, they have been reported to have distinct functions. While α1 KO mice show severe anemia due to less deformability of erythrocytes and higher sensitivity to erythrophagocytosis,[28] α2 KO mice are insulin resistant and glucose intolerant.[29] A protective role of AMPKα2 in the heart under pressure overload has also been reported.[30,31] *PRKAA2*$^{-/-}$ mice demonstrated significantly exacerbated TAC-induced ventricular hypertrophy and decreased LV ejection fraction. These results are consistent with the phenotype observed in TAC-operated knockin mice in this study.

Interestingly, TAC-operated *Bcl2l13*$^{-/-}$ mice demonstrated milder hypertrophy than *Bcl2l13*$^{+/+}$ mice, while Bcl2-L-13 (S272A) knockin mice showed more severe hypertrophy. Previous studies have reported that the promotion of mitochondrial fission

(E and F) HEK293A cells were transfected with control siRNA (siCtrl) or siAMPKα2 for 72 h, followed by transfection with an empty vector or HA-Bcl2-L-13. Forty-four hours after transfection, cells were treated with 100 nM bafilomycin A1 for 4 h and immunostained with anti-LC3B and anti-ATP synthase antibodies. Images in the box at higher magnification are shown on the right. White arrows indicate the puncta recognized as colocalized by the software. The number of LC3B dots colocalized with ATP synthase dots per cell is shown in (F). At least 20 cells were counted for each group (n = 3). Scale bar: 10 μm.

(G) Upregulation of AMPKα2 phosphorylation 5 days after TAC operation. To analyze AMPKα2-specific phosphorylation, lysates from the left ventricle were subjected to immunoprecipitation with an anti-AMPKα2 antibody followed by immunoblotting with an anti-phospho-AMPKα (Thr172) antibody. Densitometric analysis of phospho-AMPKα (Thr172) is shown in the right bar graph. The value for the WT sham group in each experiment was set to 1 (n = 3).

(H) Interaction between Bcl2-L-13 and AMPKα2 5 days after TAC. Lysates from the left ventricle were subjected to immunoprecipitation with an anti-AMPKα2 antibody. Co-precipitated Bcl2-L-13 was detected by immunoblotting. Densitometric analysis of Bcl2-L-13 is shown in the graph below. The value for the WT sham group in each experiment was set to 1 (n = 3). Results are shown as mean with 95% CI. Statistical analysis by unpaired, two-tailed t tests in (C), (D), (F), and (H) and one-way ANOVA followed by Tukey-Kramer's post hoc test in (G). All pairwise comparisons were performed. $^{*}p < 0.05$, $^{**}p < 0.01$, $^{***}p < 0.001$. ns, not significant. See also Figures S6 and S7.

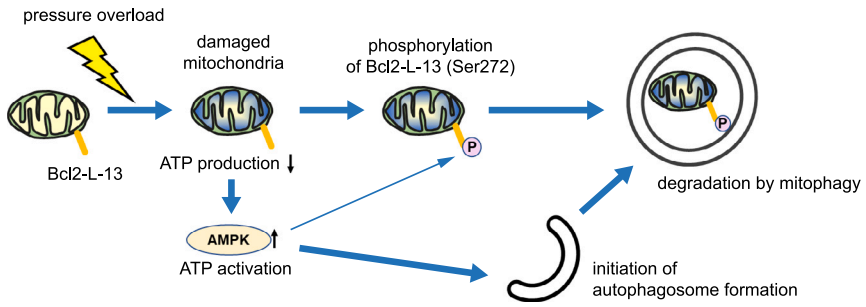

Figure 7. A model of the role of AMPK in Bcl2-L-13-mediated mitophagy under pressure overload

Pressure overload damages mitochondria, leading to decreased ATP production and subsequent activation of AMPK. Activated AMPK initiates autophagosome formation and directly phosphorylates Bcl2-L-13 for mitophagy induction.

resulted in cardiomyocyte hypertrophy.[32,33] Our previously reported *in vitro* study showed that Bcl2-L-13 knockdown induced mitochondrial elongation, while Bcl2-L-13 overexpression induced mitochondrial fission and mitophagy.[8] Although a recent study has shown that Bcl2-L-13 promotes mitophagy through Drp1-mediated mitochondrial fission in glioblastoma,[34] Bcl2-L-13 induced mitochondrial fission even in Drp1 knockdown HEK293 cells in our previous report.[8] The discrepancy might be due to differences in cell types. In addition, Bcl2-L-13 (S272A) overexpression had no effect on mitochondrial dynamics but inhibited mitophagy, suggesting that Bcl2-L-13 is involved in mitochondrial fission and mitophagy and that its phosphorylation regulates mitophagy but not fission. However, in the current study, TAC-operated knockin mice demonstrated elongated mitochondria, contrary to our expectations. In addition, sham-operated *Bcl2l13*$^{-/-}$ mice had an increased number of mitochondria with shorter long diameters compared to *Bcl2l13*$^{+/+}$ mice. We could not explain these changes based on the results of the protein analyses of fusion/fission-related molecules. Therefore, further studies regarding the mechanisms of Bcl2-L-13 mediated mitochondrial fission, including its relationship to Ser272 phosphorylation, are needed to explain the discrepancies in the mitochondrial dynamics between *in vitro* and *in vivo* models and how mitochondrial dynamics are related to pressure overload-induced cardiac hypertrophy.

In summary, Bcl2-L-13 deficiency induced the development of cardiac dysfunction, presumably due to the impairment of mitochondrial fission and mitophagy, and subsequent accumulation of damaged mitochondria. Phosphorylation of Bcl2-L-13 at Ser272 by AMPKα2 plays an important role in this process. Our findings provide the first evidence that Bcl2-L-13 has protective effects on the heart, and activation of Bcl2-L-13 through the phosphorylation at Ser272 could be a potential therapeutic target for heart failure patients. Since the involvement of calcium signaling in AMPKα2-dependent Bcl2-L-13-phosphorylation is suggested in this study, and AMPK is implicated in a wide range of metabolic pathways, it is important to clarify the entire upstream intracellular signaling cascades of AMPKα2 for the specific targeted therapy. In addition, the combination of subunit isoforms in the AMPK complex should also be taken into consideration.

Limitations of the study

We used global KO mice of Bcl2-L-13 in this study to compare the phenotype with global knockin mice used in the following experiment. However, the use of global KO mice is a limitation of the study in that we cannot rule out the effects of Bcl2-L-13 ablation in non-cardiomyocyte cells or in other organs on observed cardiac phenotypes. Cardiomyocyte-specific KO mice would help us to obtain a better understanding of the exact roles of Bcl2-L-13 in cardiomyocytes.

RESOURCE AVAILABILITY

Lead contact

Requests for further information, resources, and reagents should be directed to and will be fulfilled by the lead contact, Kinya Otsu (otsu.kinya@ncvc.go.jp).

Materials availability

The plasmids and mice generated in this study are available upon request.

Data and code availability

- All data supporting the findings of this study are available within the article and its supplemental information. Source data, including images, have been deposited in Figshare: https://doi.org/10.6084/m9.figshare.25284883 and DRYAD: https://doi.org/10.5061/dryad.9cnp5hqsx.
- This paper does not report original code.
- Any additional information required to reanalyze the data reported in this paper is available from the lead contact upon request.

ACKNOWLEDGMENTS

The work was supported by the European Research Council (692659), the British Heart Foundation (CH/11/3/29051 and RG/16/15/32294), the Fondation Leducq (RA15CVD04), JSPS KAKENHI grant 18H02807 (to K.O.), JSPS KAKENHI grants 22K16102 and 24K11215 (to T.M.), and JSPS KAKENHI grant 21K21350 (to S.O.).

AUTHOR CONTRIBUTIONS

T.M. was responsible for research design, execution, data analysis, and manuscript preparation. J.I., M.-C.R., M.T., J.M.-A., C.N., R.S., H.N., and K.M. were responsible for performing experiments and manuscript preparation. M.Z. was responsible for data analysis and manuscript preparation. S.O. was responsible for conducting and supervising experiments, data analysis, and manuscript preparation. K.N. was responsible for developing the mouse model and the supervision of experiments, data analysis, and manuscript preparation. R.F., A.M.S., O.Y., and Y.S. were responsible for data interpretation and manuscript preparation. K.O. was responsible for the supervision and design of the research, data interpretation, and manuscript preparation.

DECLARATION OF INTERESTS

The authors declare no competing interests.

STAR★METHODS

Detailed methods are provided in the online version of this paper and include the following:

- KEY RESOURCES TABLE
- EXPERIMENTAL MODEL AND STUDY PARTICIPANT DETAILS
  - Cell culture
  - Animal study
  - Generation of conventional *Bcl2l13* knockout mice
  - Generation of Bcl2-L-13 (S272A) knock-in mice
- METHOD DETAILS
  - TAC and echocardiography
  - Antibodies
  - Transfection
  - Construction of plasmids
  - Construction of HA-Bcl2-L-13 stable cell line
  - Southern blot analysis
  - Histological analysis
  - Quantitative RT–PCR
  - SDS–PAGE and western blotting
  - Immunoprecipitation
  - Sample preparation for electron microscopy
  - Electron microscopy imaging and analysis
  - siRNA library screening
  - *In vitro* kinase assay
  - ATP assay
  - AMPK activity assay
  - Isolation of mouse adult cardiomyocytes
  - MitoSOX analysis
  - Assessment of mitochondrial function
  - Mitochondrial DNA damage assay
  - Assessment of mitophagy in *in vitro*
  - Assessment of mitophagy in *in vivo* hearts
  - TUNEL staining
  - Detection of necrosis
- QUANTIFICATION AND STATISTICAL ANALYSIS

SUPPLEMENTAL INFORMATION

Supplemental information can be found online at https://doi.org/10.1016/j.celrep.2024.115001.

Received: August 15, 2023
Revised: September 25, 2024
Accepted: November 6, 2024
Published: November 23, 2024

REFERENCES

1. McDonagh, T.A., Metra, M., Adamo, M., Gardner, R.S., Baumbach, A., Böhm, M., Burri, H., Butler, J., Čelutkienė, J., Chioncel, O., et al. (2022). 2021 ESC Guidelines for the diagnosis and treatment of acute and chronic heart failure: Developed by the Task Force for the diagnosis and treatment of acute and chronic heart failure of the European Society of Cardiology (ESC) With the special contribution of the Heart Failure Association (HFA) of the ESC. Rev. Esp. Cardiol. *75*, 523. https://doi.org/10.1016/j.rec.2022.05.005.
2. Ramaccini, D., Montoya-Uribe, V., Aan, F.J., Modesti, L., Potes, Y., Wieckowski, M.R., Krga, I., Glibetić, M., Pinton, P., Giorgi, C., and Matter, M.L. (2020). Mitochondrial Function and Dysfunction in Dilated Cardiomyopathy. Front. Cell Dev. Biol. *8*, 624216. https://doi.org/10.3389/fcell.2020.624216.
3. Moyzis, A.G., Sadoshima, J., and Gustafsson, Å.B. (2015). Mending a broken heart: the role of mitophagy in cardioprotection. Am. J. Physiol. Heart Circ. Physiol. *308*, H183–H192. https://doi.org/10.1152/ajpheart.00708.2014.
4. Dikic, I., and Elazar, Z. (2018). Mechanism and medical implications of mammalian autophagy. Nat. Rev. Mol. Cell Biol. *19*, 349–364. https://doi.org/10.1038/s41580-018-0003-4.
5. Kanki, T., Wang, K., Cao, Y., Baba, M., and Klionsky, D.J. (2009). Atg32 is a mitochondrial protein that confers selectivity during mitophagy. Dev. Cell *17*, 98–109. https://doi.org/10.1016/j.devcel.2009.06.014.
6. Okamoto, K., Kondo-Okamoto, N., and Ohsumi, Y. (2009). Mitochondria-anchored receptor Atg32 mediates degradation of mitochondria via selective autophagy. Dev. Cell *17*, 87–97. https://doi.org/10.1016/j.devcel.2009.06.013.
7. Onishi, M., Yamano, K., Sato, M., Matsuda, N., and Okamoto, K. (2021). Molecular mechanisms and physiological functions of mitophagy. EMBO J. *40*, e104705. https://doi.org/10.15252/embj.2020104705.
8. Murakawa, T., Yamaguchi, O., Hashimoto, A., Hikoso, S., Takeda, T., Oka, T., Yasui, H., Ueda, H., Akazawa, Y., Nakayama, H., et al. (2015). Bcl-2-like protein 13 is a mammalian Atg32 homologue that mediates mitophagy and mitochondrial fragmentation. Nat. Commun. *6*, 7527. https://doi.org/10.1038/ncomms8527.
9. Shiba-Fukushima, K., Imai, Y., Yoshida, S., Ishihama, Y., Kanao, T., Sato, S., and Hattori, N. (2012). PINK1-mediated phosphorylation of the Parkin ubiquitin-like domain primes mitochondrial translocation of Parkin and regulates mitophagy. Sci. Rep. *2*, 1002. https://doi.org/10.1038/srep01002.
10. Wu, W., Tian, W., Hu, Z., Chen, G., Huang, L., Li, W., Zhang, X., Xue, P., Zhou, C., Liu, L., et al. (2014). ULK1 translocates to mitochondria and phosphorylates FUNDC1 to regulate mitophagy. EMBO Rep. *15*, 566–575. https://doi.org/10.1002/embr.201438501.
11. Rogov, V.V., Suzuki, H., Marinković, M., Lang, V., Kato, R., Kawasaki, M., Buljubašić, M., Šprung, M., Rogova, N., Wakatsuki, S., et al. (2017). Phosphorylation of the mitochondrial autophagy receptor Nix enhances its interaction with LC3 proteins. Sci. Rep. *7*, 1131. https://doi.org/10.1038/s41598-017-01258-6.
12. Chen, G., Han, Z., Feng, D., Chen, Y., Chen, L., Wu, H., Huang, L., Zhou, C., Cai, X., Fu, C., et al. (2014). A regulatory signaling loop comprising the PGAM5 phosphatase and CK2 controls receptor-mediated mitophagy. Mol. Cell *54*, 362–377. https://doi.org/10.1016/j.molcel.2014.02.034.
13. Kataoka, T., Holler, N., Micheau, O., Martinon, F., Tinel, A., Hofmann, K., and Tschopp, J. (2001). Bcl-rambo, a novel Bcl-2 homologue that induces apoptosis via its unique C-terminal extension. J. Biol. Chem. *276*, 19548–19554. https://doi.org/10.1074/jbc.M010520200.
14. Yoon, Y., Krueger, E.W., Oswald, B.J., and McNiven, M.A. (2003). The mitochondrial protein hFis1 regulates mitochondrial fission in mammalian cells through an interaction with the dynamin-like protein DLP1. Mol. Cell Biol. *23*, 5409–5420. https://doi.org/10.1128/MCB.23.15.5409-5420.2003.
15. Taguchi, N., Ishihara, N., Jofuku, A., Oka, T., and Mihara, K. (2007). Mitotic phosphorylation of dynamin-related GTPase Drp1 participates in mitochondrial fission. J. Biol. Chem. *282*, 11521–11529. https://doi.org/10.1074/jbc.M607279200.
16. Cribbs, J.T., and Strack, S. (2007). Reversible phosphorylation of Drp1 by cyclic AMP-dependent protein kinase and calcineurin regulates mitochondrial fission and cell death. EMBO Rep. *8*, 939–944. https://doi.org/10.1038/sj.embor.7401062.
17. Abudureyimu, M., Yu, W., Cao, R.Y., Zhang, Y., Liu, H., and Zheng, H. (2020). Berberine Promotes Cardiac Function by Upregulating PINK1/Parkin-Mediated Mitophagy in Heart Failure. Front. Physiol. *11*, ARTN565751. https://doi.org/10.3389/fphys.2020.565751.
18. Cao, Y., Xu, C., Ye, J., He, Q., Zhang, X., Jia, S., Qiao, X., Zhang, C., Liu, R., Weng, L., et al. (2019). Miro2 Regulates Inter-Mitochondrial Communication in the Heart and Protects Against TAC-Induced Cardiac Dysfunction. Circ. Res. *125*, 728–743. https://doi.org/10.1161/CIRCRESAHA.119.315432.

19. Bolte, S., and Cordelières, F.P. (2006). A guided tour into subcellular colocalization analysis in light microscopy. J Microsc-Oxford *224*, 213–232. https://doi.org/10.1111/j.1365-2818.2006.01706.x.

20. Chakrabarty, Y., Yang, Z., Chen, H., and Chan, D.C. (2024). The HRI branch of the integrated stress response selectively triggers mitophagy. Mol. Cell *84*, 1090–1100.e6. https://doi.org/10.1016/j.molcel.2024.01.016.

21. Readnower, R.D., Brainard, R.E., Hill, B.G., and Jones, S.P. (2012). Standardized bioenergetic profiling of adult mouse cardiomyocytes. Physiol. Genom. *44*, 1208–1213. https://doi.org/10.1152/physiolgenomics.00129.2012.

22. Ruas, J.S., Siqueira-Santos, E.S., Amigo, I., Rodrigues-Silva, E., Kowaltowski, A.J., and Castilho, R.F. (2016). Underestimation of the Maximal Capacity of the Mitochondrial Electron Transport System in Oligomycin-Treated Cells. PLoS One *11*, e0150967. https://doi.org/10.1371/journal.pone.0150967.

23. Scott, S.R., Singh, K., Yu, Q., Sen, C.K., and Wang, M. (2022). Sex as Biological Variable in Cardiac Mitochondrial Bioenergetic Responses to Acute Stress. Int. J. Mol. Sci. *23*, 9312. https://doi.org/10.3390/ijms23169312.

24. Zhu, Y., Massen, S., Terenzio, M., Lang, V., Chen-Lindner, S., Eils, R., Novak, I., Dikic, I., Hamacher-Brady, A., and Brady, N.R. (2013). Modulation of serines 17 and 24 in the LC3-interacting region of Bnip3 determines pro-survival mitophagy versus apoptosis. J. Biol. Chem. *288*, 1099–1113. https://doi.org/10.1074/jbc.M112.399345.

25. Egan, D.F., Shackelford, D.B., Mihaylova, M.M., Gelino, S., Kohnz, R.A., Mair, W., Vasquez, D.S., Joshi, A., Gwinn, D.M., Taylor, R., et al. (2011). Phosphorylation of ULK1 (hATG1) by AMP-activated protein kinase connects energy sensing to mitophagy. Science *331*, 456–461. https://doi.org/10.1126/science.1196371.

26. Murakawa, T., Okamoto, K., Omiya, S., Taneike, M., Yamaguchi, O., and Otsu, K. (2019). A Mammalian Mitophagy Receptor, Bcl2-L-13, Recruits the ULK1 Complex to Induce Mitophagy. Cell Rep. *26*, 338–345.e6. https://doi.org/10.1016/j.celrep.2018.12.050.

27. Liang, J., Xu, Z.X., Ding, Z., Lu, Y., Yu, Q., Werle, K.D., Zhou, G., Park, Y.Y., Peng, G., Gambello, M.J., and Mills, G.B. (2015). Myristoylation confers noncanonical AMPK functions in autophagy selectivity and mitochondrial surveillance. Nat. Commun. *6*, 7926. https://doi.org/10.1038/ncomms8926.

28. Foretz, M., Guihard, S., Leclerc, J., Fauveau, V., Couty, J.P., Andris, F., Gaudry, M., Andreelli, F., Vaulont, S., and Viollet, B. (2010). Maintenance of red blood cell integrity by AMP-activated protein kinase alpha1 catalytic subunit. FEBS Lett. *584*, 3667–3671. https://doi.org/10.1016/j.febslet.2010.07.041.

29. Viollet, B., Andreelli, F., Jørgensen, S.B., Perrin, C., Geloen, A., Flamez, D., Mu, J., Lenzner, C., Baud, O., Bennoun, M., et al. (2003). The AMP-activated protein kinase alpha2 catalytic subunit controls whole-body insulin sensitivity. J. Clin. Invest. *111*, 91–98. https://doi.org/10.1172/JCI16567.

30. Wang, B., Nie, J., Wu, L., Hu, Y., Wen, Z., Dong, L., Zou, M.H., Chen, C., and Wang, D.W. (2018). AMPKα2 Protects Against the Development of Heart Failure by Enhancing Mitophagy via PINK1 Phosphorylation. Circ. Res. *122*, 712–729. https://doi.org/10.1161/CIRCRESAHA.117.312317.

31. Zhang, P., Hu, X., Xu, X., Fassett, J., Zhu, G., Viollet, B., Xu, W., Wiczer, B., Bernlohr, D.A., Bache, R.J., and Chen, Y. (2008). AMP activated protein kinase-alpha2 deficiency exacerbates pressure-overload-induced left ventricular hypertrophy and dysfunction in mice. Hypertension *52*, 918–924. https://doi.org/10.1161/HYPERTENSIONAHA.108.114702.

32. Song, M., Mihara, K., Chen, Y., Scorrano, L., and Dorn, G.W., 2nd. (2015). Mitochondrial fission and fusion factors reciprocally orchestrate mitophagic culling in mouse hearts and cultured fibroblasts. Cell Metabol. *21*, 273–286. https://doi.org/10.1016/j.cmet.2014.12.011.

33. Pennanen, C., Parra, V., López-Crisosto, C., Morales, P.E., del Campo, A., Gutierrez, T., Rivera-Mejías, P., Kuzmicic, J., Chiong, M., Zorzano, A., et al. (2014). Mitochondrial fission is required for cardiomyocyte hypertrophy mediated by a Ca2+-calcineurin signaling pathway. J. Cell Sci. *127*, 2659–2671. https://doi.org/10.1242/jcs.139394.

34. Wang, J., Chen, A., Xue, Z., Liu, J., He, Y., Liu, G., Zhao, Z., Li, W., Zhang, Q., Chen, A., et al. (2023). BCL2L13 promotes mitophagy through DNM1L-mediated mitochondrial fission in glioblastoma. Cell Death Dis. *14*, 585. https://doi.org/10.1038/s41419-023-06112-4.

35. Johannessen, C.M., Boehm, J.S., Kim, S.Y., Thomas, S.R., Wardwell, L., Johnson, L.A., Emery, C.M., Stransky, N., Cogdill, A.P., Barretina, J., et al. (2010). COT drives resistance to RAF inhibition through MAP kinase pathway reactivation. Nature *468*, 968–972. https://doi.org/10.1038/nature09627.

36. Hu, P., Zhang, D., Swenson, L., Chakrabarti, G., Abel, E.D., and Litwin, S.E. (2003). Minimally invasive aortic banding in mice: effects of altered cardiomyocyte insulin signaling during pressure overload. Am. J. Physiol. Heart Circ. Physiol. *285*, H1261–H1269. https://doi.org/10.1152/ajpheart.00108.2003.

37. Omiya, S., Omori, Y., Taneike, M., Protti, A., Yamaguchi, O., Akira, S., Shah, A.M., Nishida, K., and Otsu, K. (2016). Toll-like receptor 9 prevents cardiac rupture after myocardial infarction in mice independently of inflammation. Am. J. Physiol. Heart Circ. Physiol. *311*, H1485–H1497. https://doi.org/10.1152/ajpheart.00481.2016.

38. Schindelin, J., Arganda-Carreras, I., Frise, E., Kaynig, V., Longair, M., Pietzsch, T., Preibisch, S., Rueden, C., Saalfeld, S., Schmid, B., et al. (2012). Fiji: an open-source platform for biological-image analysis. Nat. Methods *9*, 676–682. https://doi.org/10.1038/nmeth.2019.

39. Lam, J., Katti, P., Biete, M., Mungai, M., AshShareef, S., Neikirk, K., Garza Lopez, E., Vue, Z., Christensen, T.A., Beasley, H.K., et al. (2021). A Universal Approach to Analyzing Transmission Electron Microscopy with ImageJ. Cells *10*, 2177. https://doi.org/10.3390/cells10092177.

STAR★METHODS

KEY RESOURCES TABLE

REAGENT or RESOURCE	SOURCE	IDENTIFIER
Antibodies		
Rabbit monoclonal Anti-HA tag (clone C29F4)	Cell Signaling Technology	Cat# 3724; RRID: AB_1549585
Rabbit polyclonal anti-LC3B	Cell Signaling Technology	Cat# 2775; RRID: AB_915950
Mouse monoclonal anti-Myc Tag (clone 9B11)	Cell Signaling Technology	Cat# 2776; RRID: AB_390779
Rabbit polyclonal anti-Phospho-DRP1 (Ser637)	Cell Signaling Technology	Cat#4867; RRID: AB_10622027
Rabbit polyclonal anti-Phospho-DRP1 (Ser616)	Cell Signaling Technology	Cat# 3455; RRID: AB_2085352
Rabbit monoclonal anti-Mitofusin2 (clone D2D10)	Cell Signaling Technology	Cat# 9482; RRID: AB_2716838
Rabbit monoclonal anti-Mitofusin1 (clone D6E2S)	Cell Signaling Technology	Cat# 14739; RRID: AB_2744531
Rabbit monoclonal anti-OPA1 (clone D6U6N)	Cell Signaling Technology	Cat# 80471; RRID: AB_2734117
Mouse monoclonal anti-GAPDH (clone D4C6R)	Cell Signaling Technology	Cat# 97166; RRID: AB_2756824
Mouse monoclonal anti-α-Tubulin (clone DM1A)	Cell Signaling Technology	Cat# 3873; RRID: AB_1904178
Rabbit polyclonal anti-Parkin	Cell Signaling Technology	Cat# 2132; RRID: AB_10693040
Rabbit monoclonal anti-PINK1 (clone D8G3)	Cell Signaling Technology	Cat# 6946; RRID: AB_11179069
Rabbit polyclonal anti-AMPKα1	Cell Signaling Technology	Cat# 2795; RRID: AB_560856
Rabbit polyclonal anti-AMPKα2	Cell Signaling Technology	Cat# 2757; RRID: AB_560858
Rabbit polyclonal anati-AMPKα2	Proteintech	Cat# 18167-1-AP; RRID: AB_10695046
Rabbit polyclonal anti-BCL2L13	Proteintech	Cat# 16612-1-AP; RRID: AB_1850928
Mouse monoclonal anti-PGC1-α (1C1B2)	Proteintech	Cat# 66369-1-Ig; RRID: AB_2828002
Mouse monoclonal anti-FLAG tag (clone M2)	Sigma-Aldrich	Cat# F1804; RRID: AB_262044
Mouse monoclonal anti-α-sarcomeric actin	Sigma-Aldrich	Cat# A2172; RRID: AB_476695
Rabbit polyclonal anti-TTC11	abcam	Cat# ab96764; RRID: AB_10679033
Rabbit polyclonal anti-HMGB1	abcam	Cat# ab18256; RRID:AB_444360
Mouse monoclonal anti-ATP synthase	Life Technologies	Cat# A-21351; RRID: AB_221512
Mouse monoclonal anti-Drp1 (clone 22)	BD Transduction Laboratories	Cat# 611738; RRID: AB_399214
Sheep Anti-Mouse IgG HRP Conjugated	Amersham	Cat#NA931; RRID: AB_772210
Donkey Anti-Rabbit IgG HRP Conjugated	Amersham	Cat# NA934; RRID: AB_772206
IRDye 800CW Donkey anti-Goat IgG	LI-COR Biosciences	Cat# 926–32214; RRID: AB_621846
IRDye 680LT Goat anti-Mouse IgG	LI-COR Biosciences	Cat# 926–68020; RRID: AB_10706161
IRDye 680RD Donkey anti-Rabbit IgG	LI-COR Biosciences	Cat# 926–68073; RRID: AB_10954442
IRDye 800CW Donkey anti-Mouse IgG	LI-COR Biosciences	Cat# 926–32212; RRID: AB_621847
IRDye 800CW Goat anti-Rabbit IgG	LI-COR Biosciences	Cat# 926–32211; RRID: AB_621843
Goat anti-Mouse IgM (Heavy chain) Cross-Adsorbed Secondary Antibody, Alexa Fluor™ 568	Thermo Fisher Scientific	Cat# A-21043; RRID:AB_2535712

(*Continued on next page*)

Continued

REAGENT or RESOURCE	SOURCE	IDENTIFIER
Goat anti-Rabbit IgG (H + L) Highly Cross-Adsorbed Secondary Antibody, Alexa Fluor™ 488	Thermo Fisher Scientific	Cat# A-11034; RRID:AB_2576217
Donkey anti-Goat IgG (H + L) Cross-Adsorbed Secondary Antibody, Alexa Fluor™ 568	Thermo Fisher Scientific	Cat# A-11057; RRID:AB_2534104
Chicken Anti-Goat IgG (H + L) Antibody, Alexa Fluor 647 Conjugated	Thermo Fisher Scientific	Cat# A21469; RRID:AB_10374877
Donkey anti-Mouse IgG (H + L) Highly Cross-Adsorbed Secondary Antibody, Alexa Fluor™ 568	Thermo Fisher Scientific	Cat# A10037; RRID:AB_11180865
Bacterial and virus strains		
Genlantis TurboCells BL21Competent Cells	Gelantis	AMS.C302020
Chemicals, peptides, and recombinant proteins		
RNAi MAX	Invitrogen	Cat# 13778030
ScreenFect A	Wako	Cat# 299-73203
Penicillin-Streptomycin-Glutamine	Gibco	Cat# 10378016
geneticin	Gibco	Cat# 10131-027; CAS: 108321-42-2
Bafilomycin A1	LC Laboratories	Cat# B-1080; CAS: 88899-55-2
ECL Prime Western Blotting Detection Reagent	GE Healthcare Life Science	Cat# RPN2232
Lumigen ECL Ultra	Lumigen	Cat# TMA-100
CCCP	Sigma-Aldrich	Cat# C2759; CAS: 555-60-2
ProLong Gold Antifade Mountant with DAPI	Thermo Fisher Scientific	Cat# P36935
MitoSox	Life Technologies	Cat# M36008
fluorescein isothiocyanate-conjugated lectin	Sigma	L4895
protease inhibitor cocktail	Cell Signaling Technology	#5871
phosphatase inhibitor cocktail	Cell Signaling Technology	#5870
Dynabeads Protein A for Immunoprecipitation	Thermo Fisher Scientific	Cat# 1001D
GST Spin Purification Kit	Thermo Scientific Pierce	Cat# 11804025
PreScission Protease	GE Healthcare Lifescience	–
AMPK A2/B1/G1 Recombinant Human Protein	Thermo Fisher Scientific	Cat# PV4674
CAMK2B (CaMKII Beta) Recombinant Human Protein	Thermo Fisher Scientific	Cat# PV4205
ERK4 Recombinant Protein	SignalChem	Cat# M30-34G-20
FASTK Recombinant Protein	SignalChem	Cat# F01-10G-05
Haspin Recombinant Protein	SignalChem	Cat# G10-11G-05
IRAK2 Recombinant Protein	SignalChem	Cat# I10-10BG-05
NLK Recombinant Human Protein	Thermo Fisher Scientific	Cat# PV4309
CDC42 BPA (MRCKA) Recombinant Human Protein	Thermo Fisher Scientific	Cat# PV4398
Recombinant human PKM2 protein	abcam	Cat# ab89364
MAP3K7/MAP3K7IP1 (TAK1-TAB1) Recombinant Human Protein	Thermo Fisher Scientific	Cat# PV4394
ACVR2A Human Protein	Thermo Fisher Scientific	Cat# PV6124
AAK1 Recombinant Human Protein	Thermo Fisher Scientific	Cat# A30967
RIPK3 Recombinant Protein	SignalChem	Cat# R09-10G-05

(*Continued on next page*)

Continued

REAGENT or RESOURCE	SOURCE	IDENTIFIER
PKAc beta, active	Eurofins Pharma Discovery	Cat# 15-007
BAPTA-AM	TCI chemicals	Cat# T2845
Dorsomorphin	FUJIFILM Wako	Cat# 044-33751
Quercetin	Sigma-Aldrich	Cat# Q4951
N-acetylcysteine	Sigma-Aldrich	Cat# A9165: CAS: 616-91-1
Critical commercial assays		
ATP Assay Kit	abcam	Cat# ab83355
In situ Apoptosis Detection Kit	Takara Bio	Cat# MK500
AMPK Kinase Assay Kit	Cyclex	Cat# CY-1182
DNeasy Blood & Tissue Kit	QIAGEN	Cat# 69504
mouse Real-time PCR Mitochondrial DNA Damage Analysis Kit	Detroit R&D	Cat# DD2M
Deposited data		
Raw and analyzed data	This paper; Figshare	Tables S5, S6 and S7; https://doi.org/10.6084/m9.fig.share.25284883
Images from primary and second screening	This paper; Dryad	https://doi.org/10.5061/dryad.9cnp5hqsx
Experimental models: Cell lines		
Human: HEK293A Cell line	Invitrogen	Cat# R70507; RRID: CVCL_6910
Experimental models: Organisms/strains		
Bcl2-L-13 knockout mice	This paper	N/A
Bcl2-L-13 S272A knockin mice	This paper	N/A
Oligonucleotides		
Silencer™ Human Kinase siRNA Library	ThermoFisher Scientific	Cat# A30079
siRNA: AMPKα1	ThermoFisher Scientific	Cat# AM51551, siRNA ID: 768
siRNA: AMPKα2	ThermoFisher Scientific	Cat# AM51331, siRNA ID: 771
Negative Control No. 1 siRNA	ThermoFisher Scientific	Cat# 4390843
Recombinant DNA		
pDONR223-PRKAA2	Johannessen et al.[35]	Addgene; Cat# 23671
HA-Bcl2-L-13-pcDNA3.1	Murakawa et al.[8]	N/A
myc-AMPKα2-pcDNA3.1	This paper	N/A
pGEX-Bcl2-L-13	This paper	N/A
Software and algorithms		
ImageJ (Version 1.52p)	National Institue of Health, USA	https://imagej.nih.gov/ij/index.html
Image Studio	LI-COR Biosciences	N/A
ImageQuantTL v7.0	GE Healthcare Life Sciences	–
Graphpad Prism 9	GraphPad Software	N/A

EXPERIMENTAL MODEL AND STUDY PARTICIPANT DETAILS

Cell culture

HEK293A cells (RRID: CVCL_6910) were obtained from Invitrogen and were grown in Dulbecco's modified Eagle's medium (D5671, Sigma) supplemented with 10% fetal bovine serum and 1% penicillin-streptomycin-glutamine (10378016, Gibco) at 37°C under 5% CO_2. The sex of the cells was female.

Animal study

All animal studies were approved by the King's College London Ethical Review Process Committee and UK Home Office (project license PPL70/7260) and the Animal Research Committee of Osaka University. All experiments were carried out in accordance with the U.K. Animals (Scientific Procedures) Act 1986, and the associated guidelines, Directive 2010/63/EU for animal experiments and in accordance with the Guidelines for Animal Experiments of Osaka University and the Japanese Animal Protection and Management Law. The authors complied with the ARRIVE (Animal Research: Reporting of *In Vivo* Experiments) guidelines.

Generation of conventional *Bcl2l13* knockout mice

The mouse C57BL/6J BAC genomic library (BACPAC Resources Center) was used to generate a homology sequence for the *Bcl2l13* gene targeting vector. The homology sequence was generated by high-fidelity polymerase chain reaction (PCR) and cloned into the targeting vector containing the *DT-loxP-PGK-Neo-loxP* cassette. The targeting vector was electroporated into ES cells (F1; SVJ129 and C57BL/6J). The transfected ES clones were subsequently selected for neomycin resistance. Southern blotting and karyotyping analyses were performed to obtain ES clones exhibiting the desired homologous recombination and normal karyotype. These targeted ES clones were injected into blastocyst mouse embryos to generate chimeric mice. The chimeric mice were crossed with C57BL/6J mice to validate germ-line transmission. The offspring with floxed *Bcl2l13* mice were crossed with transgenic mice expressing *Cre* recombinase under the control of the β-actin promoter (*βActin-Cre* mice) in the C57BL/6J background to generate conventional *Bcl2l13* gene deletion. Mice were backcrossed onto a C57BL/6J background for six generations. Genotyping was determined using the following primer sets: 5′- TGT GGA TAC CAT TCT CTT CCT GT-3' and 5′-AAG TTG GCT TTT GAG ACG TAC C-3′ to amplify the deleted allele, and 5′- GGT TTT TAT TGA CCT GGT GAG C -3' and 5′- AAG TTG GCT TTT GAG ACG TAC C -3' to amplify the wild-type allele.

To generate double knockout mice of *Bcl2l13* and *Park2*, *Bcl2l13*$^{-/-}$ mice were crossed with *Park2*$^{-/-}$ mice in the C57BL/6J background. *Park2*$^{-/-}$ mice were purchased from The Jackson Laboratory.

Generation of Bcl2-L-13 (S272A) knock-in mice

Bcl2-L-13 (S272A) knock-in phospho-deficient mice were generated by genOway. The S272A mutation was introduced by replacing the TCC (serine) codon with the GCA (alanine) codon, located in exon 8 of the *Bcl2l13* gene. The targeting vector containing a *Neo* expression cassette for positive selection and a DTA expression cassette for negative selection was electroporated in ES cells. Selected ES cell clones were then assessed by PCR and Southern blot analysis to validate the presence of the correct recombination event. These ES clones were injected into blastocysts to create chimeric mice. Chimeric mice were subsequently mated with C57BL/6 *Cre* deleter mice to excise the *Neo* selection cassette and generate heterozygous mice carrying the Neo-excised knock-in point mutant allele. The obtained progeny were genotyped by PCR, and the recombinase-mediated excision event was further validated by Southern blot analysis. Genotyping was done using the forward primer 5′- GAA AAT CAT TCT TAG CTA ACC TCA GTT TCA GGA G -3' and the reverse primer 5′- TGA GGC TGG ACA GAA TAT TGA GAC TGT TG -3'. For all experiments, wild-type and homozygotes were generated exclusively by breeding heterozygotes. To avoid potential sex-specific differences, all experiments used male mice. Mice were randomly assigned to control or TAC groups, and studies were performed unblinded regarding mouse genotypes.

METHOD DETAILS

TAC and echocardiography

The 8 to 12-week-old mice were subjected to TAC using a 25-gauge needle.[36] Sham-operated mice underwent the same operation without aortic constriction. A 6–0 silk suture was placed around the transverse aorta (between the innominate and left common carotid artery) and tied loosely in a single knot. A pre-sterilized, blunt-end 25-gauge needle was placed within the knot alongside the transverse aorta. The knot was tightened fully with an additional knot, and the blunt-end needle was removed.

Echocardiography was conducted using the Vevo 2100 system (Visual Sonics) on conscious mice.[37] Non-invasive measurements of the tail blood pressure were also performed on conscious mice using a BP Monitor for rats and mice (Muromachi Kikai).

Antibodies

The following primary antibodies were purchased: anti-HA tag (#3724), anti-myc tag (#2276), anti-LC3B (#2775), anti-pDrp1 Ser637 (#4867), anti-pDrp1 Ser616 (#3455), anti-Mfn2 (#9482), anti-Mfn1 (#14739), anti-OPA1 (#80471), anti-GAPDH (#97166), α-tubulin (#3873), anti-Parkin (#2132), anti-PINK1 (#6946), anti-AMPKα1 (#2795), and anti-AMPKα2 (#2757) from Cell Signaling Technology, anti-Bcl2-L-13 (16612-1-AP), anti-PGC1α (66369-1-AP) and anti-AMPKα2 (18167-1-AP) from Proteintech, anti-FLAG (F1804), and anti-α-sarcomeric actin (A2172) from Sigma-Aldrich, anti-Fis1 (ab96764), and anti-HMGB1 (ab18256) from Abcam, anti-ATP synthase (A-21351, Life Technologies), and anti-Drp1 (611738, BD Transduction Laboratories). Anti-phospho-Bcl2-L-13 (Ser272) was generated by the Medical Research Council. A peptide corresponding to amino acid residues 267–277 of mouse Bcl2-L-13, in which phosphorylation site (serine) is substituted to aspartic acid (SLGPEDWQQIA), was injected into a sheep. The antisera were affinity-purified on phosphopeptide–agarose, followed by chromatography on the corresponding dephospho peptide–agarose column to remove antibodies that recognize dephosphorylated Bcl2-L-13.

Secondary antibodies used were the following: Amersham ECL Mouse IgG (NA931) and Amersham ECL Rabbit IgG (NA934) from GE Healthcare, and IRDye 800CW Donkey anti-Goat IgG (H + L) (926–32214), IRDye 680LT Goat anti-Mouse IgG (H + L) (926–68020), IRDye 680RD Donkey anti-Rabbit IgG (H + L) (926–68073), IRDye 800CW Donkey anti-Mouse IgG (H + L) (926–32212) and IRDye 800CW Goat anti-Rabbit IgG (H + L) (926–32211) from LI-COR Biosciences, and Goat anti-mouse IgM (Heavy chain) Alexa Fluor 568 (A21043), Goat anti-rabbit IgG (H + L) Alexa Fluor 488 (A11034), Donkey anti-goat IgG (H + L) Alexa Fluor 568 (A11057), Donkey anti-Mouse IgG (H + L) Alexa Fluor 568 (A10037), and Chicken anti-goat IgG (H + L) Alexa Fluor 647 (A21469) from Invitrogen.

Transfection

Transient transfections were performed using ScreenFect A (299–73203, Wako). After 48 h, cells were subjected to analysis unless otherwise indicated. For siRNA-mediated knockdown, cells were transfected with 20 nM AMPKα1 siRNA (AM51551, siRNA ID: 768) and 20 nM AMPKα2 siRNA (AM51331, siRNA ID: 771) from Thermo Fisher using 3.75 μL/mL of RNAiMAX (13778150, Invitrogen). The non-targeting siRNA control (4390843) was obtained from Thermo Fisher. After 72 h of transfection, cells were subjected to analysis unless otherwise indicated.

Construction of plasmids

To generate HA-Bcl2-L-13-pcDNA3.1, N-terminal hemagglutinin (HA) -tagged mouse Bcl2-L-13 was cloned into pcDNA3.1.[8] The pDONR223-PRKAA2 was a gift from William Hahn & David Root (Addgene plasmid # 23671).[35] To generate myc-AMPKα2-pcDNA3.1, human AMPKα2 was amplified from pDONR223-PRKAA2 with forward (5′- AGC AGA ATT CGA TGG CTG AGA AGC AGA AGC AC -3') and reverse (5′- AGC AGG ATC CTC AAC GGG CTA AAG TAG TAA T -3') primers. The amplified fragment was directly inserted into pCR-Blunt II-TOPO and then subcloned into pcDNA3.1. To obtain pGEX-Bcl2-L-13, Bcl2-L-13 (1–407) including HA tag was amplified from HA-Bcl2-L-13-pcDNA3.1 with forward (5′- AGC AGG ATC CGC CGC CAT GGA GTA CCC ATA CGA CGT A -3') and reverse (5′- AGC ACT CGA GTC AGG CCT TGC CCT CGG CGG GCA GGC CAC T -3') primers. The amplified fragment was directly inserted into pCR-Blunt II-TOPO and subcloned into the BamHI/XhoI site of pGEX-6P-2.

Construction of HA-Bcl2-L-13 stable cell line

The HA-Bcl2-L-13-pcDNA3.1 plasmid was transfected into HEK293A cells using ScreenFect A. After 48 h, the cells were passaged, and 1 mg/mL G418 for selection was added 24 h later. After 14 days, the single colonies were transferred to 24-well plates and expanded.

Southern blot analysis

Genomic DNAs (gDNAs) were purified from embryonic stem cells using the Qiagen DNeasy kit (Qiagen) according to the manufacturer's instructions. Approximately 10 μg of gDNA was digested with restriction enzymes and ran in a 1% agarose gel for 20 h at 30 V. Genomic DNA fragments were transferred from the gel via capillary action to a nylon membrane (0.45 μm pore) using alkaline transfer. The membrane was then exposed to a source of UV light for 3 min for cross-linking. Probes for hybridization were labeled with ^{32}P-dCTP using the Amersham Megaprime DNA labeling system (GE Healthcare). Hybridization was performed at 68°C overnight using the QuikHyb Rapid Hybridization solution (Agilent).

Histological analysis

Left ventricle samples were embedded in an OCT compound (Thermo Fisher Scientific Inc) and then immediately frozen in liquid nitrogen. The samples were cut into 5 μm-thick sections. The sections were fixed with acetone for hematoxylin–eosin and Masson's trichrome staining and with 4% paraformaldehyde for wheat germ agglutinin staining. For wheat germ agglutinin staining, heart samples were stained with fluorescein isothiocyanate-conjugated lectin (L4895, Sigma) to measure the cross-sectional area of cardiomyocytes.

Images were captured by a fluorescence microscope (BZ-X700, Keyence). The fibrosis fraction and cardiomyocyte cross-sectional area were examined using ImageJ (National Institutes of Health; Version 1.52p).

Quantitative RT–PCR

Total RNA was isolated from the left ventricles using the TRIzol reagent (Thermo Fisher Scientific). The mRNA expression levels were determined by quantitative reverse transcription PCR using a SuperScript IV reverse transcriptase (Thermo Fisher Scientific) for reverse transcription and a PowerUp SYBR Green PCR Master Mix (Thermo Fisher Scientific) for the quantitative reverse transcription PCR reaction with the following PCR primers: forward 5′- TCG TCT TGG CCT TTT GGC T -3′ and reverse 5′- TCC AGG TGG TCT AGC AGG TTC T -3′ for *Nppa*, forward 5' -AAG TCC TAG CCA GTC TCC AGA -3′ and reverse 5′- GAG CTG TCT CTG GGC CAT TTC -3′ for *Nppb*, and forward 5′- ATG ACA ACT TTG TCA AGC TCA TTT -3′ and reverse 5′- GGT CCA CCA CCC TGT TGC T -3′ for *Gapdh*. All data were normalized to the *Gapdh* mRNA content and expressed as a fold increase over the control group.

SDS–PAGE and western blotting

Cells were washed in ice-cold PBS and lysed in lysis buffer (50 mM Tris-HCl, 137 mM NaCl, 1 mM EDTA, 10% glycerol, 1% Triton X-100, a protease inhibitor cocktail (#5871, Cell Signaling), and a phosphatase inhibitor cocktail (#5870, Cell Signaling), pH 8.0) on ice.

For mouse tissue, samples were homogenized and lysed in lysis buffer (25 mM Tris-HCl, 150 mM NaCl, 1% deoxycholic acid sodium salt, 0.1% SDS, 1.0% NP-40 substitute, pH 7.6) on ice. Proteins were subjected to SDS–PAGE and transferred to a nitrocellulose membrane. Membranes were incubated with primary antibodies overnight at 4°C, followed by incubations with secondary antibodies at room temperature (RT) for 1 h. The blot was developed using an infrared imaging system (ODYSSEY CLx, LI-COR Biosciences) or ImageQuant LAS4000mini (GE Healthcare Life Sciences). Image Studio software (LI-COR Biosciences) or ImageQuantTL v7.0 (GE Healthcare Life Sciences) was used for quantitative analysis to evaluate protein expression levels.

Immunoprecipitation

To investigate if Bcl2-L-13 forms a complex with AMPKα2, an immunoprecipitation experiment was conducted. Lysates from LV were precleared with 30 μL of magnetic beads-coupled protein A (1001D, Invitrogen) and 1 μg of rabbit immunoglobulin G. Precleared lysates were subjected to immunoprecipitation using 1 μg of the anti-AMPKα2 antibody or rabbit immunoglobulin G and 30 μL of magnetic beads-coupled protein A at 4°C for 4 h. The precipitated complexes were washed three times with lysis buffer for immunoblotting by an anti-Bcl2-L-13 antibody.

Sample preparation for electron microscopy

Before perfusion fixation, 5 U heparin and 50 mg pentobarbital/kg body weight were intraperitoneally administered to mice. Perfusion was performed using an infusion syringe pump (Harvard Apparatus). To avoid blood clots forming during fixation, the blood was washed from the circulatory system via perfusion with a buffer containing 0.1% $NaNO_2$ and 2.5% polyvinylpyrrolidone (PVP) in 100 mM PIPES(pH 7.2). Mouse hearts were fixed by perfusion fixation using 2% glutaraldehyde (EM grade, Sigma-Aldrich) and 2% formaldehyde (EMS) in 100 mM PIPES(pH 7.2) containing 0.1% $NaNO_2$ and 2.5% PVP. The hearts were excised and kept in a fixative solution on ice for 1 h before dissection. The left ventricular free walls were dissected from the fixed hearts and cut into 1–2 mm^3 blocks. Post-fixation was carried out for 1 h at 4°C in 2% OsO_4 in 100 mM sodium cacodylate (pH 7.2). Blocks were thoroughly washed with double-distilled water and then dehydrated using ethanol series (10%, 50%, 70%, and 100% ethanol) and propylene oxide. The blocks were embedded in Agar100 epoxy resin (Agar Scientific) following overnight infiltration. Tissue blocks were sectioned using a Leica Ultracut (EM UC 7) ultramicrotome. Sections were collected on Maxtaform type H6 copper finder grids (Agar Scientific) coated in-house with Pioloform and carbon films or on commercially available Formvar/Carbon slot grids (Agar Scientific). Sections were stained with UranyLess and Reynolds Lead Citrate (TAAB Laboratories Equipment Ltd.).

Electron microscopy imaging and analysis

For each experimental group, three to four animals were included in the analysis and random sampling of the left ventricle was ensured by sectioning three blocks from each mouse. Tissue sections were imaged using a 120 kV JEOL JEM-transmission electron microscope (TEM) equipped with the JEOL Ruby CCD camera. Ultrastructural assessment of the cardiac tissue was carried out on 70-nm thick sections. For assessing mitochondrial morphological parameters, areas consisting of longitudinal muscle fibers were imaged at a nominal magnification of 5000× (283.5 pixels/μm). Only inter-myofibrillar mitochondria were included in the frequency distribution analysis. Micrographs were analyzed using the open-source image processing software FIJI.[38,39] Using the Freehand selection tool, inter-myofibrillar mitochondria were traced. The long diameter is the primary axis of the best-fitting ellipse to the traced pixels. In an animal, 504 to 728 mitochondria were measured and three to four animals were evaluated in each group. Frequency distribution was calculated in Microsoft Excel. GraphPad Prism was used to generate violin plots and to assess the difference between distributions of mitochondria morphological parameters. Statistical significance was evaluated using the Kruskal-Wallis statistical test. Numerical data of the measurement of mitochondria are provided in Table S5.

siRNA library screening

For the primary screen, the Silencer Human Kinase siRNA Library (three siRNAs per gene) targeting 708 genes (ThermoFisher Scientific, A30079) was used. 96-well tissue culture plates were prearrayed with 3.6 pmol of siRNA and 0.24 μL of Lipofectamine RNAiMAX (Invitrogen) per well. Reverse transfection of 3,000 HEK293A cells stably expressing HA-Bcl2-L-13 was performed with a 30 nM final concentration of siRNAs. A non-targeting siRNA control was used as the negative control.

Seventy-two hours post-transfection, 15 μM CCCP was added to induce mitophagy together with 100 nM bafilomycin A1 for 4 h. Cells were fixed with 4% paraformaldehyde in PBS and permeabilized with 0.1% Triton X-100 in PBS. Cells were then incubated with the anti-phospho-Bcl2-L-13 (Ser272) antibody overnight at 4°C, followed by incubation with anti-goat Alexa 568 for 1 h at RT. After washing, images were obtained by automated scanning using a fluorescence microscope (BZ-X700, Keyence; ×20 objective lens, × 2 digital zoom, nine view fields per well). For quantification of phospho-Bcl2-L-13 (Ser272) puncta, local maxima were determined using the "find maxima" function of the ImageJ software package. We chose target genes that demonstrated an over 60% reduction compared with positive control well in at least one out of three siRNAs or an over 40% reduction in at least two siRNAs for the secondary screen. Furthermore, Z scoring was used to confirm our screening criteria. We selected genes with a Z score greater than 1.5 as hits. We carried forward genes that fulfilled each of those criteria. The Z′ factor for the primary screening was calculated using the DMSO-treated samples (positive control for inhibition) and control siRNA-treated samples (negative control for inhibition). The Z′ factor for the primary screen was calculated to be 0.91.

For the secondary screen, HEK293A cells stably expressing HA-Bcl2-L-13 were transfected with candidate siRNA using RNAiMAX. A non-targeting siRNA control was used as the positive control. Seventy-two hours after the transfection, cells were treated with 15 μM CCCP and 100 nM bafilomycin A1 for 4 h. Cells were fixed and permeabilized with methanol for 10 min at −20°C. Cells were then incubated with rabbit anti-LC3B antibody and mouse anti-ATP synthase antibody overnight at 4°C, followed by incubation with secondary antibodies for 1 h at RT. After washing, cells were mounted with ProLong Gold Antifade Mountant and analyzed using a Nikon Ti-Eclipse inverted microscope (Nikon). Mitophagy was manually evaluated by counting the number of ATP synthase dots colocalized with LC3B dots. At least 20 cells were quantified. Target genes that demonstrated an over 40% reduction compared with the positive control were selected for the *in vitro* kinase assay. We also evaluated mitophagy using the

JACoP plugin of ImageJ for colocalization analysis.[19,20] We chose genes with a *Z* score greater than 1.0 as hits. The Z′ factor for the secondary screening was calculated using the DMSO-treated samples (positive coFfntrol for inhibition) and control siRNA-treated samples (negative control for inhibition). The Z′ factor for the secondary screen was calculated to be 0.76. We carried forward all genes that were selected under either of those two evaluation methods. Numerical data of the primary and secondary screens are provided in Table S6.

In vitro kinase assay

The GST-fusion proteins of HA-Bcl2-L-13 or HA-Bcl2-L-13 (S272A) were induced in the BL21 *Escherichia coli* strain (DE3; AMS.C302020, Genlantis) transfected with pGEX-Bcl2-L-13 or pGEX-Bcl2-L-13 (S272A) by adding 1 mM isopropyl-β-D-thiogalactoside (10724815001, Roche) for 3.5 h. Bacteria were lysed with PBS containing 1 mg/mL lysozyme (10536394, Fisher Bioreagents), 30 U/ml Benzonase (E1014-5KU, Sigma), 1 mM dithiothreitol, 1 mM EDTA, 1% Triton X-100 and protease inhibitors. GST-Bcl2-L-13 or GST-Bcl2-L-13 (S272A) were purified using the GST Spin Purification Kit (11804025, Thermo Scientific Pierce). The GST tag was cleaved using the PreScission Protease (10196324, GE Healthcare Lifescience) on a column.

For the *in vitro* kinase assay, 0.5 μg purified kinases were mixed with 0.5 μg bacteria-synthesized proteins from HA-Bcl2-L-13 or HA-Bcl2-L-13 (S272A), 1 mM ATP, and the kinase reaction buffer (50 mM Tris-HCl, 10 mM $MgCl_2$, 2 mM dithiothreitol, pH7.4).

After incubation at 30°C for 30 min, the reaction mix underwent Western blotting. Purified kinases were purchased from SignalChem or Thermo Fisher Scientific.

ATP assay

Approximately 10 mg of the left ventricle was homogenized in ice-cold 2 N perchloric acid (PCA). Then, excess PCA was precipitated via the addition of ice-cold 2 M KOH, and the pH was adjusted to 6.5–8.0. The ATP concentrations of the deproteinized samples were measured using the ATP Assay Kit from Abcam (ab83355) according to the manufacturer's instructions. Fluorometric assay (Ex/Em = 535/587 nm) was performed using the TECAN INFINITE 200 plate reader. Results were normalized to the weight of each sample.

AMPK activity assay

HEK293A cells stably expressing HA-Bcl2-L-13 were transfected with siAMPKα1 for 72 h and then treated with DMSO or 15 μM CCCP. Cells were lysed in lysis buffer (50 mM Tris-HCl, 137 mM NaCl, 1 mM EDTA, 10% glycerol, 1% Triton X-100, protease inhibitor cocktail (#5871, Cell Signaling), phosphatase inhibitor cocktail (#5870, Cell Signaling), pH 8.0). Five mg of lysate was resuspended in 90 μL AMPK kinase assay buffer (Cyclex, CY-1182). After a 30-min incubation at 30°C with the substrate peptide, IRS-1 S789, the activity of AMPK was analyzed according to the manufacturer's instructions.

Isolation of mouse adult cardiomyocytes

The hearts were quickly excised from anesthetized mice and cannulated via the aorta. Then hearts were perfused for 1 min at 37°C with a perfusion buffer containing 120 mM NaCl, 5.4 mM KCl, 1.6 mM $MgCl_2$, 1.2 mM NaH_2PO_4, 5.6 mM glucose, 20 mM $NaHCO_3$, and 5 mM taurine (Sigma-Aldrich), followed by perfusion with collagenase buffer containing 1.2 mg/mL collagenase type 2 (Worthington Biochemical Corporation), and 0.016 mg/mL protease type XIV (P-5147, Sigma-Aldrich). Isolated cardiomyocytes were plated onto laminin (23017-015, Invitrogen)-coated plates and cultured in Minimum Essential Medium Eagle (MEM; M5650, Sigma-Aldrich) supplemented with 2.5% FBS and L-Glutamine–Penicillin–Streptomycin solution (G6784, Sigma-Aldrich).

MitoSOX analysis

Isolated mouse adult cardiomyocytes were plated onto laminin-coated glass-based dishes. Cells were stained with 5 μM MitoSOX (M36008, Life Technologies) and 150 nM MitoTracker Green for 30 min before confocal microscopic analysis was carried out using a Nikon Ti-Eclipse inverted microscope (Nikon) equipped with a Yokogawa CSU-X1-M2 spinning disk unit (Yokogawa) and an Andor *Neo* sCMOS camera (Andor Technology).

Assessment of mitochondrial function

The oxygen consumption of adult mouse cardiomyocyte cultures was quantified using an extracellular flux analyzer (Seahorse, Agilent Technologies). Cardiomyocytes were isolated five days after the TAC operation and cultured on laminin-coated Seahorse XFe24 culture plates (100,000 cells/well). Basal OCR and maximal OCR were analyzed with the sequential administration of 1 μM oligomycin, 2 μM Carbonyl cyanide 4-(trifluoromethoxy) phenylhydrazone (FCCP) and 2 μM rotenone and 4 μM antimycin A.

Mitochondrial DNA damage assay

Total DNA was extracted from TAC-operated mouse LV using DNeasy Blood & Tissue Kit (69504, QIAGEN). Mitochondrial DNA damage was assessed using a mouse Real-time PCR Mitochondrial DNA Damage Analysis Kit (DD2M, Detroit R&D). The kit measures levels of mitochondrial DNA damage by replicating 8.2 kb mtDNA. If there is damage to the DNA, PCR cannot go through. Thus, higher long QPCR product formation represents less DNA damage. Samples (5 ng/uL DNA) were subjected to PCR reaction, after which PCR reaction product was subjected to real-time PCR. The quantification of the products was calculated from the standard curve using an 8.2 kb mtDNA standard supplied with the kit.

Assessment of mitophagy in *in vitro*

HEK293A cells were transfected with siRNA using RNAiMAX. Seventy-two hours after the initial treatment, cells were split and transfected with the expression plasmids using ScreenFect A according to the manufacturer's instructions. Forty-four hours after the second treatment, 100 nM bafilomycin A1 was added. Four hours later, cells were fixed and permeabilized with methanol for 10 min at −20°C. Cells were incubated with primary antibodies overnight at 4°C followed by incubation with secondary antibodies for 1 h at RT. After washing, cells were mounted with ProLong Gold Antifade Mountant (P36935, Invitrogen) and analyzed using a Nikon Ti-Eclipse inverted microscope (Nikon) equipped with a Yokogawa CSU-X1-M2 spinning disk unit (Yokogawa) and an Andor *Neo* sCMOS camera (Andor Technology).

To visualize the mitochondria and autophagosomes, cells were immunostained with anti-ATP synthase and anti-LC3B antibodies. Mitophagy was evaluated by counting the number of ATP synthase dots colocalized with LC3B dots. The JACoP plugin of ImageJ was used for colocalization analysis. At least 20 cells were quantified for each group.[19,20]

Assessment of mitophagy in *in vivo* hearts

Left ventricle samples were embedded in the OCT compound (Thermo Fisher Scientific Inc) and immediately frozen in liquid nitrogen. The samples were sectioned into 5 μm-thickness and fixed with methanol for 10 min at −20°C. For detection of mitophagy, mitochondria, and autophagosomes were immunostained using anti-ATP synthase and anti-LC3B antibodies. Mitophagy was estimated by counting the number of ATP synthase dots colocalized with LC3B dots. More than 30 view fields per sample were obtained using the FV3000 confocal microscope (Olympus).

TUNEL staining

Frozen heart sections were stained with *In situ* Apoptosis Detection Kit (MK500, Takara Bio) and anti-α-sarcomeric actin antibody (A2172, Sigma-Aldrich) followed by the secondary antibody Alexa Fluor 568 Anti-Mouse IgM (A21043, Invitrogen). Samples were mounted with ProLong Gold Antifade Reagent with DAPI (P36962, Invitrogen). Five view fields per sample were obtained using a fluorescence microscope (BZ-X700, Keyence) and counted signals from TUNEL staining colocalized with nuclei.

Detection of necrosis

For immunohistochemical analysis of necrosis, frozen heart sections (5 μm-thickness) were fixed in buffered 4% paraformaldehyde. The primary and secondary antibody used was a polyclonal rabbit antibody to HMGB1 (ab18256, Abcam, 1:100 dilution) and anti-rabbit IgG Alexa Fluor 488 conjugated antibody (A11034, Invitrogen, 1:100 dilution). Heart sections were also incubated with a mouse monoclonal antibody to α-sarcomeric actin and were then mounted with ProLong Gold Antifade Reagent with DAPI. Five view fields per sample were obtained using a fluorescence microscope (BZ-X700, Keyence) and evaluated HMGB1 and nucleus to calculate the percentage of HMGB1-negative cardiomyocytes.

QUANTIFICATION AND STATISTICAL ANALYSIS

The number of independent biological repeats (*n*) is shown in the figure legends. No prior estimation of sample sizes or test for normal distribution was conducted. Results are shown as mean with 95% CI. Statistical analyses were performed using GraphPad Prism 9 (GraphPad Software). Paired data were evaluated by unpaired, two-tailed *t* test. A one-way analysis of variance (ANOVA) followed by Tukey–Kramer's *post hoc* test was used for multiple comparisons. A value of $p < 0.05$ was considered statistically significant. Source data for statistical analysis are provided in Table S7.

Cell Reports, Volume *43*

Supplemental information

AMPK regulates Bcl2-L-13-mediated mitophagy induction for cardioprotection

Tomokazu Murakawa, Jumpei Ito, Mara-Camelia Rusu, Manabu Taneike, Shigemiki Omiya, Javier Moncayo-Arlandi, Chiaki Nakanishi, Ryuta Sugihara, Hiroki Nishida, Kentaro Mine, Roland Fleck, Min Zhang, Kazuhiko Nishida, Ajay M. Shah, Osamu Yamaguchi, Yasushi Sakata, and Kinya Otsu

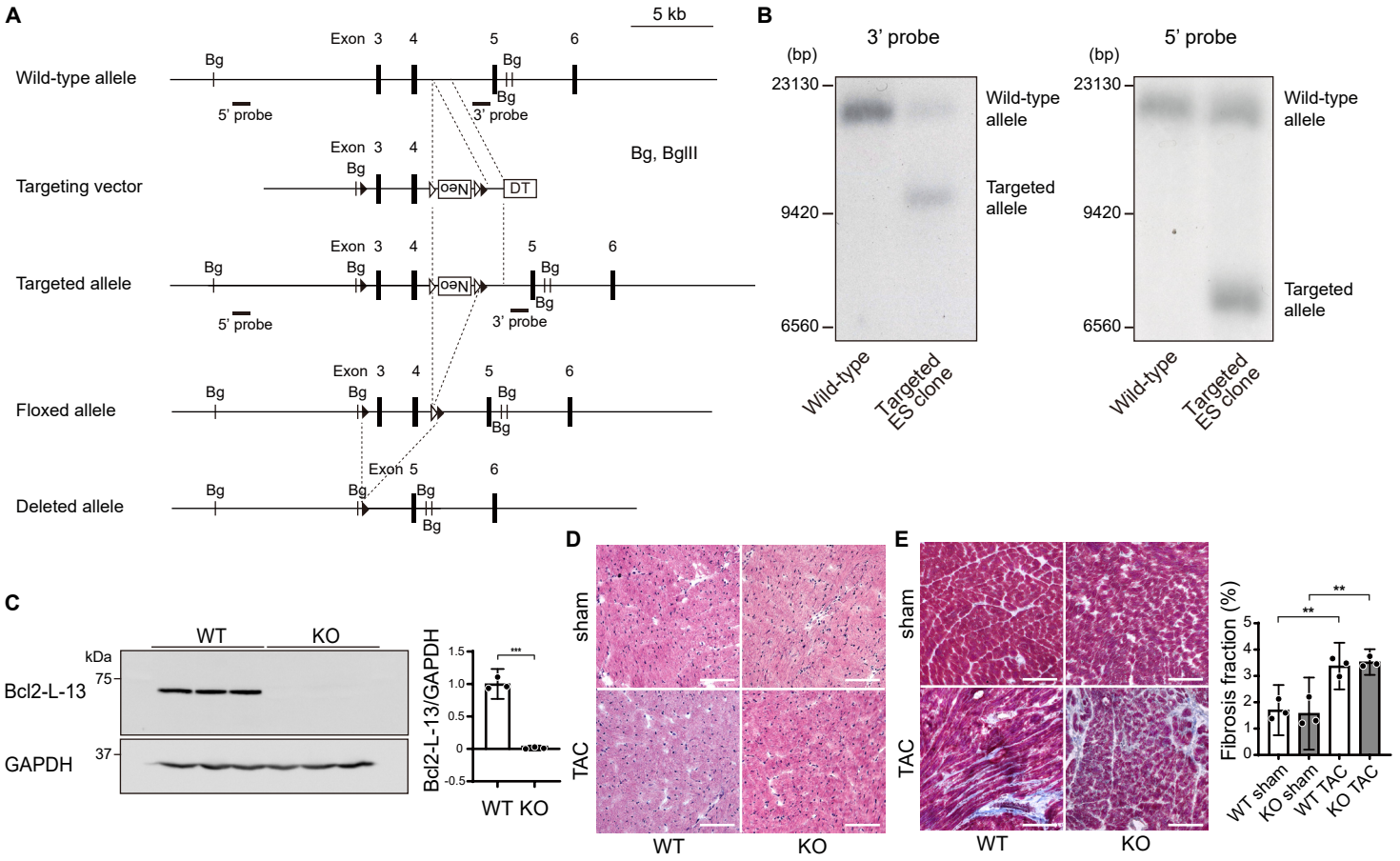

Figure S1. Targeted modification of the *Bcl2l13* gene, and histological analyses of *Bcl2l13*$^{-/-}$ mice four weeks after TAC, related to Figure 1

(A) Schematic structures of genomic *Bcl2l13* sequences, targeting vector, targeted allele, floxed allele, and *Bcl2l13*$^{-/-}$ (deleted) allele (from top to bottom). The black and white arrowheads represent *loxP* and flippase recognition target sites, respectively. The targeting construct includes the PGK-neo cassette (*Neo*) flanked by flippase recognition target sites and a diphtheria toxin (*DT*) gene. The bar-labeled probe corresponds to the sequence used for Southern blotting analysis in (B). Bg, BglII restriction site.

(B) Genomic analysis of ES cells. Genomic DNA was isolated from ES cells, digested with BglII, and analyzed via Southern blotting with 3' and 5' probes.

(C) Protein expression levels of Bcl2-L-13 in *Bcl2l13*$^{+/+}$ (WT) and *Bcl2l13*$^{-/-}$ (KO) hearts. Left ventricular homogenates from *Bcl2l13*$^{+/+}$ and *Bcl2l13*$^{-/-}$ mice were analyzed by Western blotting. The bar graph shows densitometric analysis. The average value for WT mice was set to 1 (n = 3).

(D) Hematoxylin-eosin-stained heart sections. Scale bar, 100 μm.

(E) Masson's trichrome-stained heart sections. Scale bar, 100 μm. Quantitative analysis of fibrosis fraction is shown in the bar graph (n = 3).

Results are shown as mean with 95% CI. Statistical analysis by unpaired, two-tailed *t*-test in (C) and a one-way ANOVA followed by Tukey–Kramer's *post hoc* test in (E). All pairwise comparisons were performed in Tukey–Kramer's *post hoc* test. $^{**}P < 0.01$, $^{***}P < 0.001$.

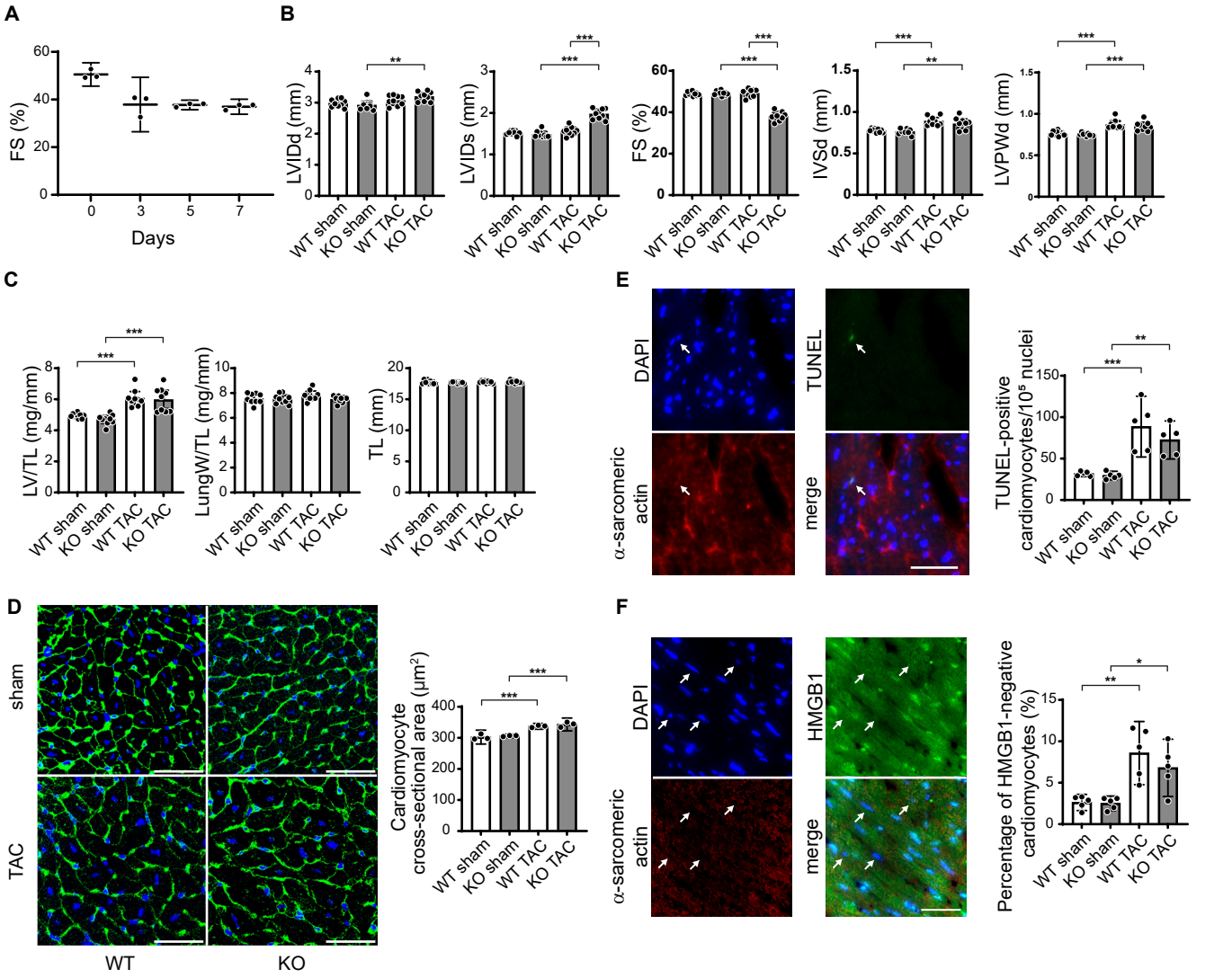

Figure S2. Analyses of *Bcl2l13*$^{-/-}$ mice five days after TAC, related to Figure 2.
(A) Analysis of fractional shortening after TAC operation in *Bcl2l13*$^{-/-}$ mice. Each data point represents the mean with 95% CI of 3 independent biological replicates.
(B and C) Echocardiographic parameters are shown in (B), and physiological parameters are shown in (C). *n* = 10.
(D) Wheat germ agglutinin-stained heart sections. Scale bar, 50 μm. Cardiomyocyte cross-sectional areas were measured by tracing the outline of 100 myocytes in the non-fibrotic area of each section (*n* = 3).
(E) Representative images of TUNEL-staining (green) in the heart sections. Arrows indicate a TUNEL-positive nucleus. Scale bar, 50 μm. Red, α-sarcomeric actin; blue, DAPI. The right graph shows a quantitative analysis of TUNEL-positive cardiomyocytes. (*n* = 5).
(F) Immunofluorescence analysis of HMGB1 (green) in the heart after TAC (*n* = 5). Arrows indicate HMGB1-negative nuclei. Scale bar, 50 μm. Red, α-sarcomeric actin; blue, DAPI. The right graph shows the percentage of HMGB1-negative cardiomyocytes.
Results are shown as mean with 95% CI. Statistical analysis by one-way ANOVA followed by Tukey–Kramer's *post hoc* test. All pairwise comparisons were performed. **P* < 0.05, ***P* < 0.01, ****P* < 0.001.

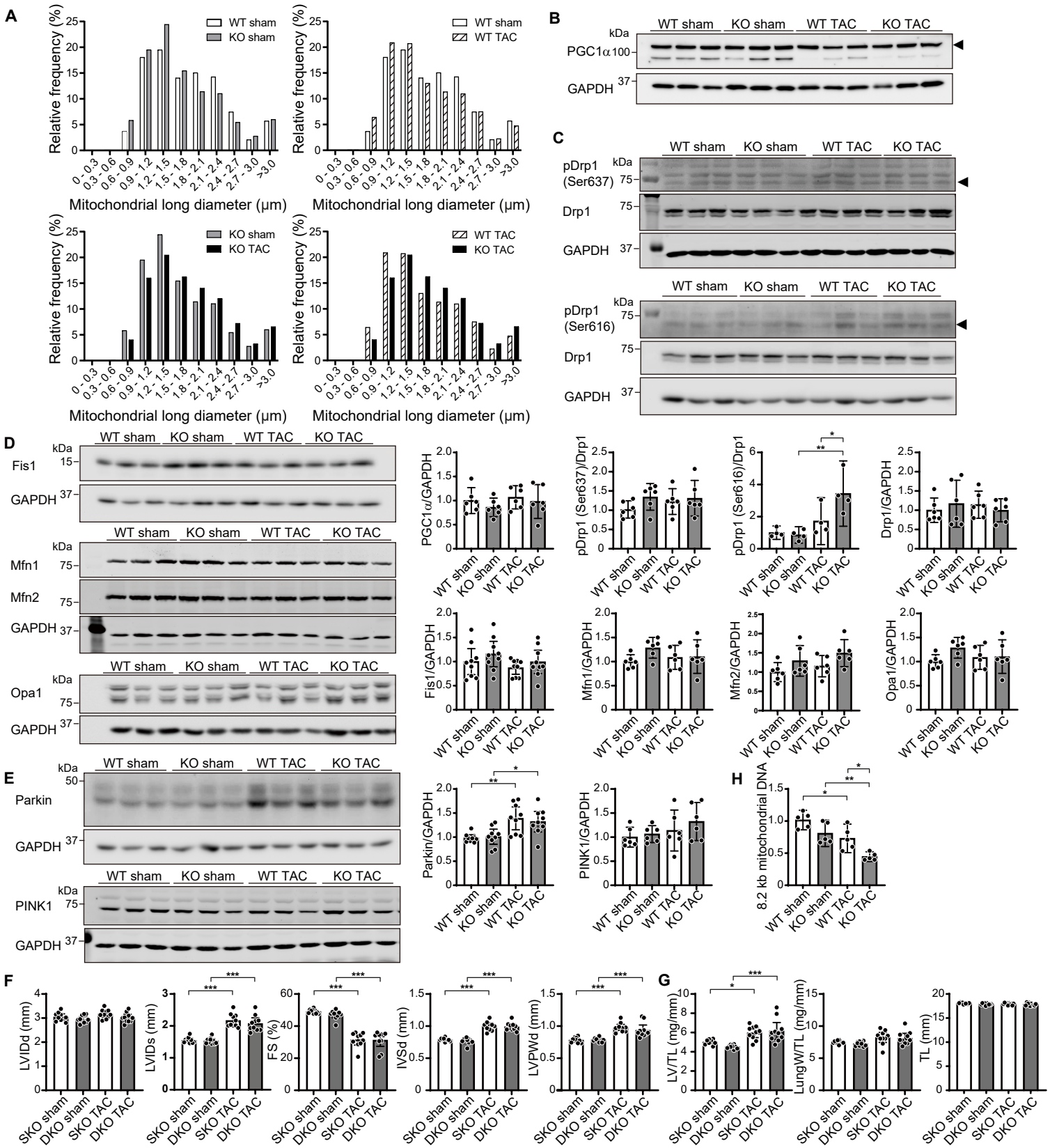

Figure S3. Ultrastructural and biochemical analyses of *Bcl2l13*$^{-/-}$ mice five days after TAC and echocardiographic and physiological analyses of *Bcl2l13*$^{-/-}$*Prk2*$^{-/-}$ mice, related to Figure 2.

(A) A histogram visualizing the distribution of the long diameter of mitochondria measured in Figure 2B.

(B-E) Heart extracts were immunoblotted with the indicated antibodies (n = 4 - 9). Densitometric analysis is shown in the bar graphs. The average value for the WT sham group was set to 1.

(F and G) *Bcl2l13*$^{-/-}$*Prk2*$^{+/+}$ (SKO) and *Bcl2l13*$^{-/-}$*Prk2*$^{-/-}$ (DKO) mice were subjected to TAC. The mice were analyzed four weeks after the TAC operation (n = 10). Echocardiographic parameters are shown in (F), and physiological parameters are shown in (G).

(H) mitochondrial DNA (mtDNA) damage was assessed by measurement of the level of replicated 8.2 kb mtDNA using mouse Real-time PCR Mitochondrial DNA Damage Analysis Kit. The damage to the mtDNA results in the inhibition of PCR of 8.2 kb mtDNA. The average value for the WT sham group was set to 1. n = 5.

Results are shown as mean with 95% CI. Statistical analysis by one-way ANOVA followed by Tukey–Kramer's *post hoc* test. All pairwise comparisons were performed. *P< 0.05, **P < 0.01, ***P < 0.001.

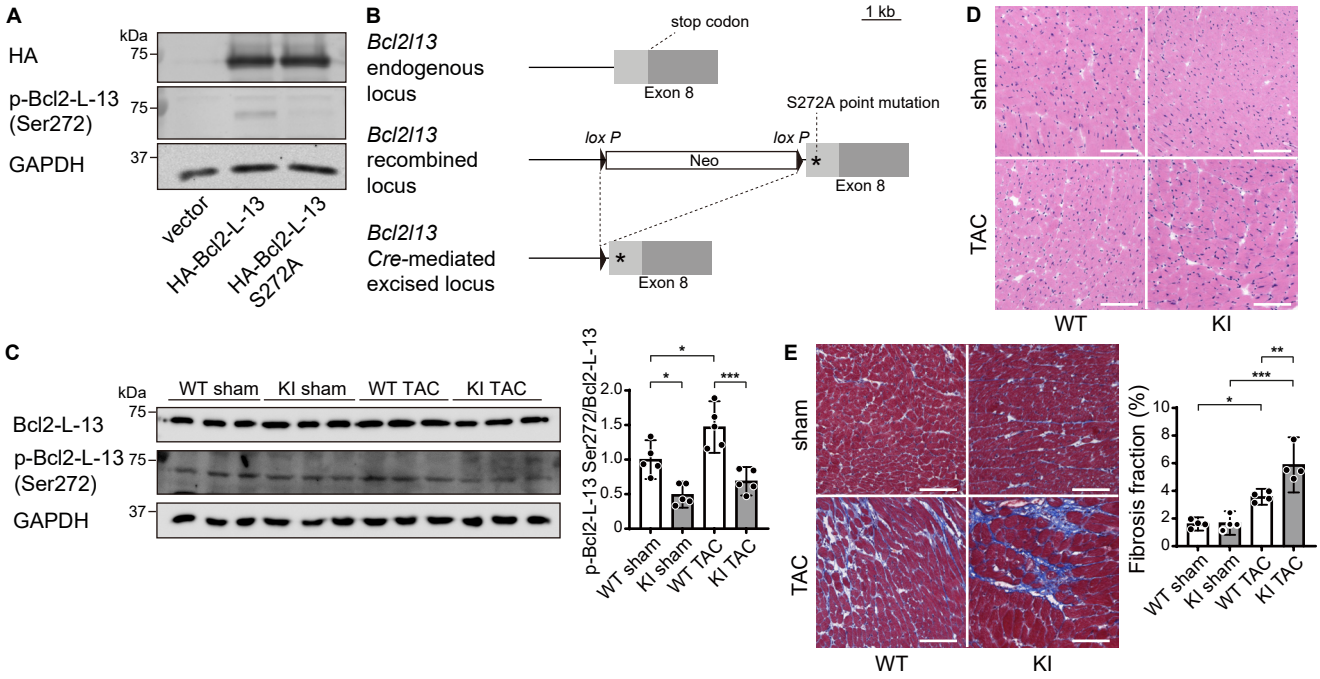

Figure S4. Histological and protein analyses in Bcl2-L-13 (S272A) knock-in mice four weeks after TAC, related to Figure 4

(A) Validation of the anti-phosho-Bcl2-L-13 (Ser272) antibody. Lysates from HEK293A cells transfected with empty vector, HA-Bcl2-L-13 or HA-Bcl2-L-13 (S272A) were subjected to immunoblotting.

(B) Schematic representation of the selected targeting strategy. Hatched rectangles represent Bcl2l13 coding sequences, grey rectangles indicate non-coding exon portions, black arrowheads indicate *loxP* sites, and asterisk indicate the inserted mutation.

(C) Heart extracts from *Bcl2L13*$^{WT/WT}$ (WT) or *Bcl2L13*$^{S272A/S272A}$ (KI) mice were immunoblotted with the indicated antibodies. Densitometric analysis is shown in the bar graph. The average value in the WT sham group was set to 1. $n = 5$.

(D) Hematoxylin-eosin-stained heart sections. Scale bar, 100 μm.

(E) Masson's trichrome-stained heart sections. Scale bar, 100 μm. Quantitative analysis of fibrosis fraction is shown in the bar graph ($n = 4$).

Results are shown as mean with 95% CI. Statistical analysis by one-way ANOVA followed by Tukey–Kramer's *post hoc* test. All pairwise comparisons were performed. **P*< 0.05, ***P* < 0.01, ****P* < 0.001.

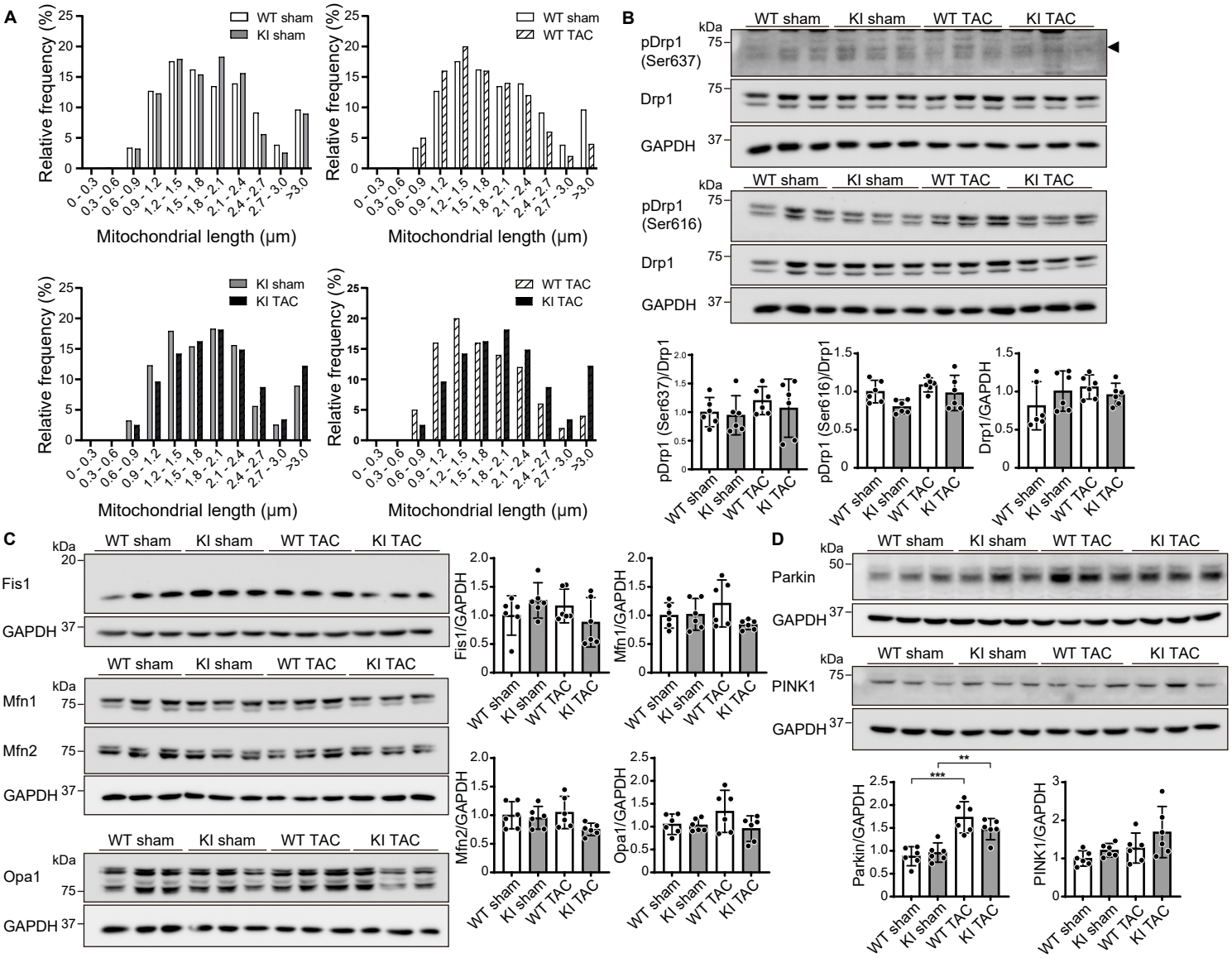

Figure S5. Ultrastructural and protein analyses in Bcl2-L-13 (S272A) knock-in mice five days after TAC, related to Figure 5

(A) A histogram visualizing the distribution of the long diameter of mitochondria measured in Figure 5A.

(B-D) Heart extracts were immunoblotted with the indicated antibodies. Densitometric analysis is shown in the bar graphs. The average value in the WT sham group was set to 1. $n = 6$.

Results are shown as mean with 95% CI. Statistical analysis by one-way ANOVA followed by Tukey–Kramer's *post hoc* test. All pairwise comparisons were performed. *$P < 0.05$, ***$P < 0.001$.

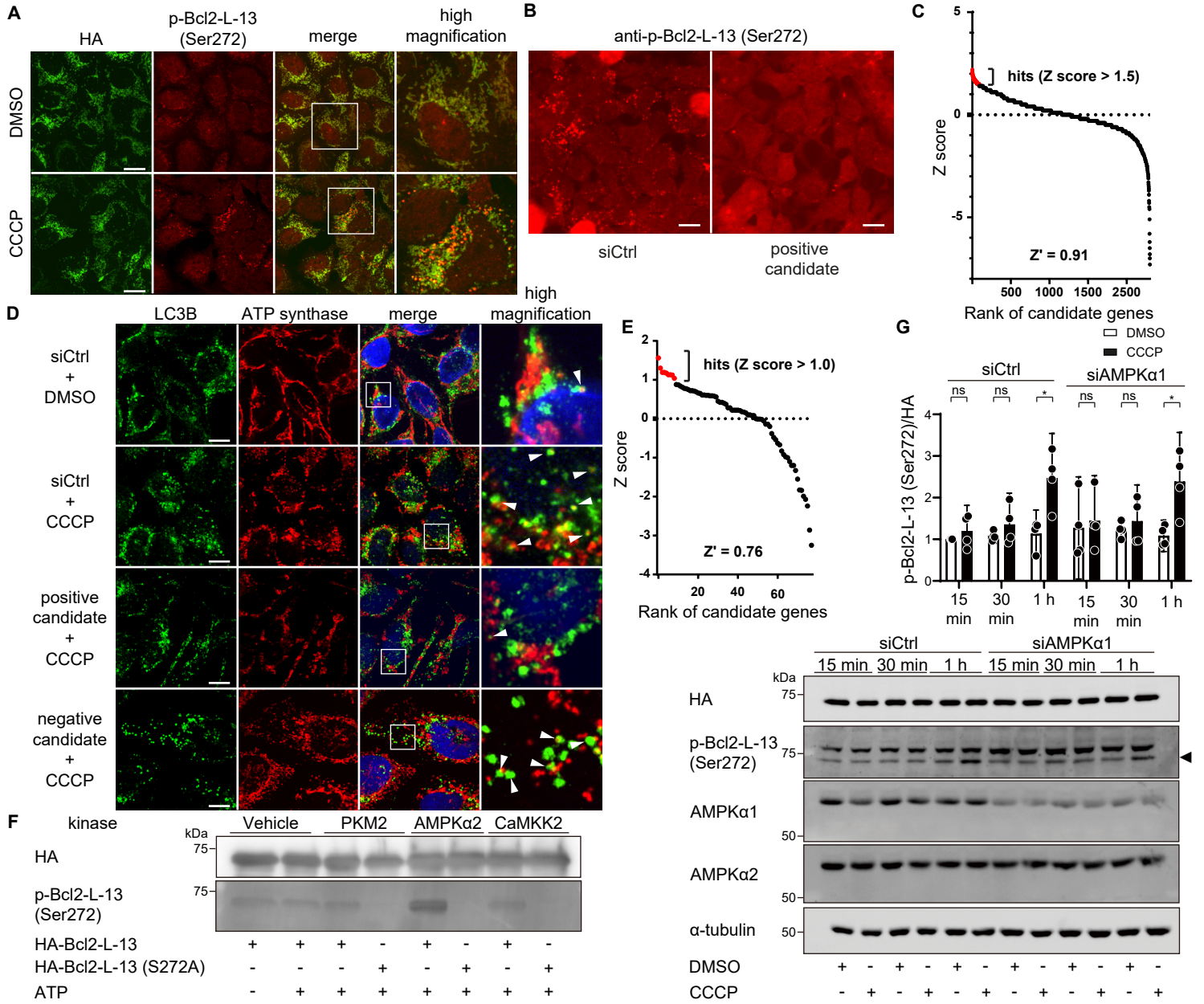

Figure S6. Screening of the responsible kinase of Bcl2-L-13 at Ser272, related to Figure 6

(A) HEK293A cells stably expressing HA-Bcl2-L-13 were treated with 15 μM CCCP and 100 nM bafilomycin A1 for four hours. Cells were fixed and immunostained with anti-phospho-Bcl2-L-13 (Ser272) and anti-HA antibodies for confocal microscopy. The boxed area is shown at higher magnification in the right panel. Scale bar, 20 μm.

(B) Representative images acquired in the primary screening. Cells were transfected with the indicated siRNAs. Seventy-two hours after transfection, cells were treated with 15 μM CCCP and 100 nM bafilomycin A1 for four hours and immunostained with an anti-phospho-Bcl2-L-13 (Ser272) antibody for automated scanning using a fluorescence microscope. For quantification of phospho-Bcl2-L-13 (Ser272)-positive dots, local maxima were determined using the “find maxima” function of the ImageJ. Scale bar, 20 μm.

(C) The candidate genes are ranked according to their Z score in the primary screening. The hits shown in red dots were chosen based on a Z score of greater than 1.5. The Z’ factor for the primary screening was calculated using the DMSO-treated samples (positive control for inhibition) and control siRNA-treated samples (negative control for inhibition).

(D) Representative images acquired in the secondary screening. HEK293A cells were transfected with the indicated siRNAs. Seventy-two hours after transfection, cells were treated with 15 μM CCCP and 100 nM bafilomycin A1 for four hours and immunostained with anti-LC3B and anti-ATP synthase antibodies for confocal microscopy. Images in the box at higher magnification are shown in the right panels. Arrowheads indicate the puncta recognized as colocalized by the software. Scale bar, 10 μm.

(E) The candidate genes are ranked according to their Z score in the secondary screening. The hits shown in red dots were chosen based on a Z score of greater than 1.0. The Z’ factor for the secondary screening was calculated using the DMSO-treated samples and control siRNA-treated samples.

(F) *In vitro* kinase assay. Bacterial synthesized HA-Bcl2-L-13 or HA-Bcl2-L-13 (S272A) was mixed with purified candidate proteins and ATP. After 30 minutes of incubation at 37°C, the reaction mix was subjected to Western blotting using an anti-phospho-Bcl2-L-13 antibody.

(G) The effect of AMPKα1 knockdown on CCCP-induced Bcl2-L-13 phosphorylation. HEK293A cells stably expressing HA-Bcl2-L-13 were transfected with the control siRNA (siCtrl) or siAMPKα1 for 72 hours. Cells were then treated with DMSO or 15 μM CCCP for the indicated times, and cell lysates were subjected to Western blot analysis. Densitometric analysis of phospho-Bcl2-L-13 (Ser272) is shown in the bar graph. The value for the siCtrl transfection and 15-minute DMSO treatment group in each experiment was set to 1 (n = 4). Results are shown as mean with 95% CI. Statistical analysis by unpaired, two-tailed t-test. *P < 0.05. ns: not significant.

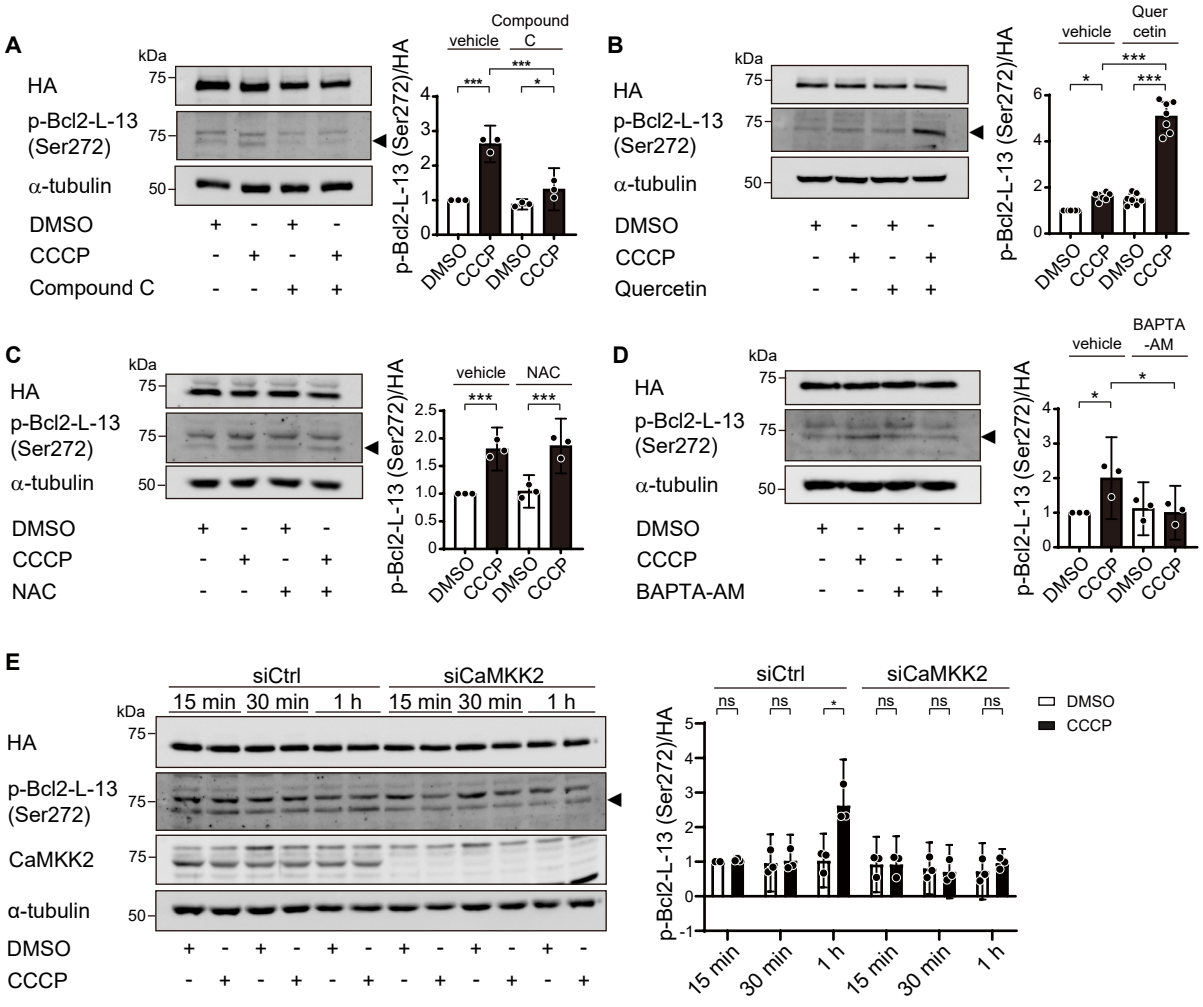

Figure S7. Regulation of the phosphorylation of Bcl2-L-13 (Ser272), related to Figure 6

(A-D) The effect of indicated drugs (10 μM Compound C, or 100 μM Quercetin, 10 μM N-Acetyl-L-cysteine (NAC), 10 μM BAPTA-AM) on CCCP-induced Bcl2-L-13 phosphorylation. HEK293A cells stably expressing HA-Bcl2-L-13 were treated with DMSO or CCCP and indicated drugs for one hour, and cell lysates were subjected to Western blot analysis. Densitometric analysis of phospho-Bcl2-L-13 (Ser272) is shown in the bar graph. The value for the DMSO and vehicle treatment group in each experiment was set to 1 (n = 3 - 7).

(E) The effect of CaMKK2 knockdown on CCCP-induced Bcl2-L-13 phosphorylation. HEK293A cells stably expressing HA-Bcl2-L-13 were transfected with the control siRNA (siCtrl) or siCaMKK2 for 72 hours. Cells were then treated with DMSO or 15 μM CCCP for the indicated times, and cell lysates were subjected to Western blot analysis. Densitometric analysis of phospho-Bcl2-L-13 (Ser272) is shown in the bar graph. The value for the siCtrl transfection and 15-minute DMSO treatment group in each experiment was set to 1 (n = 3).

Results are shown as mean with 95% CI. Statistical analysis by one-way ANOVA followed by Tukey–Kramer's *post hoc* test in (A-D) and unpaired, two-tailed *t*-tests in (E). All pairwise comparisons were performed. *P < 0.05, **P < 0.01, ***P < 0.001. ns, not significant.

Table S1. Physiological and echocardiographic parameters in 10-week-old *Bcl2l13*$^{+/+}$ and *Bcl2l13*$^{-/-}$ mice at baseline, related to Figure 1

	Bcl2l13$^{+/+}$ (*n* = 9)		*Bcl2l13*$^{-/-}$ (*n* = 8)		
	mean	**95% CI**	**mean**	**95% CI**	
Body weight (g)	**24.2**	**22.8 to 25.6**	**23.5**	**23.5 to 24.7**	***P* = 0.8700**
Blood pressure (mmHg)	**93**	**83 to 102**	**96**	**89 to 102**	***P* = 0.5393**
Heart rate (bpm)	**703**	**675 to 732**	**693**	**666 to 719**	***P* = 0.5230**
Heart weight / TL (mg/mm)	**6.7**	**6.3 to 7.1**	**6.5**	**6.1 to 6.9**	***P* = 0.4474**
Lung weight / TL (mg/mm)	**7.6**	**7.2 to 7.9**	**7.4**	**7.3 to 7.5**	***P* = 0.4604**
TL (mm)	**17.5**	**17.3 to 17.7**	**17.6**	**17.5 to 17.8**	***P* = 0.1633**
IVSd (mm)	**0.75**	**0.73 to 0.77**	**0.76**	**0.73 to 0.79**	***P* = 0.3686**
LVIDd (mm)	**2.95**	**2.84 to 3.05**	**3.01**	**2.92 to 3.10**	***P* = 0.3033**
LVIDs (mm)	**1.48**	**1.43 to 1.53**	**1.52**	**1.46 to 1.58**	***P* = 0.2405**
LVPWd (mm)	**0.74**	**0.73 to 0.75**	**0.76**	**0.74 to 0.78**	***P* = 0.1522**
FS (%)	**49.8**	**48.9 to 50.7**	**49.5**	**48.6 to 50.4**	***P* = 0.5898**

TL, tibia length; IVSd, end-diastolic interventricular septum thickness; LVIDd, end-diastolic left ventricular internal dimension; LVIDs, end-systolic left ventricular internal dimension; LVPWd, end-diastolic left ventricular posterior wall thickness; FS, fractional shortening. Paired data were evaluated by Student's *t*-test.

Table S2. Physiological and echocardiographic parameters in 10-week-old *Bcl2l13*$^{WT/WT}$ and *Bcl2l13*$^{S272A/S272A}$ mice at baseline, related to Figure 4

	Bcl2l13$^{WT/WT}$ (*n* = 8)		*Bcl2l13*$^{S272A/S272A}$ (*n* = 8)		
	mean	**95% CI**	**mean**	**95% CI**	
Body weight (g)	**25.2**	**24.3 to 26.2**	**25.7**	**24.2 to 27.1**	***P* = 0.5590**
Blood pressure (mmHg)	**97**	**86 to 107**	**102**	**94 to 110**	***P* = 0.3863**
Heart rate (bpm)	**738**	**711 to 765**	**719**	**697 to 742**	***P* = 0.2412**
Heart weight / TL (mg/mm)	**6.9**	**6.5 to 7.2**	**6.8 ± 0.2**	**6.4 to 7.2**	***P* = 0.8436**
Lung weight / TL (mg/mm)	**7.5**	**7.3 to 7.7**	**7.5**	**7.2 to 7.8**	***P* = 0.9157**
TL (mm)	**17.8**	**17.4 to 18.2**	**17.8**	**17.6 to 18.0**	***P* > 0.9999**
IVSd (mm)	**0.77**	**0.75 to 0.79**	**0.76**	**0.74 to 0.78**	***P* = 0.8506**
LVIDd (mm)	**3.04**	**2.88 to 3.19**	**2.92**	**2.73 to 3.10**	***P* = 0.2565**
LVIDs (mm)	**1.54**	**1.45 to 1.64**	**1.50**	**1.44 to 1.57**	***P* = 0.4208**
LVPWd (mm)	**0.75**	**0.74 to 0.77**	**0.76**	**0.74 to 0.77**	***P* = 0.6617**
FS (%)	**49.2**	**48.1 to 50.4**	**49.1**	**48.2 to 50.0**	***P* = 0.8546**

TL, tibia length; IVSd, end-diastolic interventricular septum thickness; LVIDd, end-diastolic left ventricular internal dimension; LVIDs, end-systolic left ventricular internal dimension; LVPWd, end-diastolic left ventricular posterior wall thickness; FS, fractional shortening. Paired data were evaluated by Student's *t*-test.

Table S3. Candidate list after the 1st screen, related to Figure 6

Gene symbol	Gene ID	Gene name
AAK1	22848	AP2-associated kinase 1
ACVR1B	91	activin A receptor, type IB
ACVR2A	92	activin A receptor, type IIA
ADCK5	203054	aarF domain containing kinase 5
ADRBK1	156	adrenergic, beta, receptor kinase 1
AK1	203	adenylate kinase 1
AK5	26289	adenylate kinase 5
AKAP7	9465	A kinase (PRKA) anchor protein 7
ANKK1	255239	ankyrin repeat and kinase domain containing 1
AURKC	6795	aurora kinase C
CAMK2A	815	calcium/calmodulin-dependent protein kinase (CaM kinase) II alpha
CAMK2N1	55450	calcium/calmodulin-dependent protein kinase I
CAMK1G	57172	calcium/calmodulin-dependent protein kinase IG
CAMKK2	10645	calcium/calmodulin-dependent protein kinase kinase 2, beta
CDC42BPA	8476	CDC42 binding protein kinase alpha (MRCK)
CERKL	375298	ceramide kinase-like
C9orf96	169436	chromosome 9 open reading frame 96
CNKSR1	10256	connector enhancer of kinase suppressor of Ras 1
CDC42BPA	8476	cyclin-dependent kinase 10
CDKL1	8814	cyclin-dependent kinase-like 1 (CDC2-related kinase)
DAPK2	23604	death-associated protein kinase 2
DCK	1633	deoxycytidine kinase
DGUOK	1716	deoxyguanosine kinase
EPHA3	2042	EPH receptor A3
FASTK	10922	Fas-activated serine/threonine kinase
FGFRL1	53834	fibroblast growth factor receptor-like 1
FRAP1	2475	FK506 binding protein 12-rapamycin associated protein 1

Table S3. Candidate list after the 1st screen (continued).

Gene symbol	Gene ID	Gene name
FLT1	2321	fms-related tyrosine kinase 1 (vascular endothelial growth factor/vascular permeability factor receptor)
FLT3	2322	fms-related tyrosine kinase 3
GALK1	2584	galactokinase 1
GSG2	83903	germ cell associated 2 (haspin)
HGS	9146	hepatocyte growth factor-regulated tyrosine kinase substrate
IPPK	64768	inositol 1,3,4,5,6-pentakisphosphate 2-kinase
IHPK3	117283	inositol hexaphosphate kinase 3
IRAK2	3656	interleukin-1 receptor-associated kinase 2
LMTK3	114783	lemur tyrosine kinase 3
LOC375133	375133	-
LOC389599	389599	-
MARK4	57787	MAP/microtubule affinity-regulating kinase 4
MAGI3	260425	membrane associated guanylate kinase, WW and PDZ domain containing 3
MAST2	23139	microtubule associated serine/threonine kinase 2
MAPK15	225689	mitogen-activated protein kinase 15
MAPK4	5596	mitogen-activated protein kinase 4 (ERK4)
MAP3K12	7786	mitogen-activated protein kinase kinase kinase 12
MAP3K7	6885	mitogen-activated protein kinase kinase kinase 7 (TAK1)
MAP4K5	11183	mitogen-activated protein kinase kinase kinase kinase 5
MLKL	197259	mixed lineage kinase domain-like
NLK	51701	nemo-like kinase
NTRK1	4914	neurotrophic tyrosine kinase, receptor, type 1
NME9	347736	NME/NM23 family member 9
NUAK1	9891	NUAK family, SNF1-like kinase, 1
PI4KB	5298	phosphatidylinositol 4-kinase, catalytic, beta
PLXNB3	5365	plexin B3
PRKCA	5578	protein kinase C, alpha

Table S3. Candidate list after the 1st screen (continued).

Gene symbol	Gene ID	Gene name
PRKAA2	5563	5'-AMP-activated protein kinase (AMPK) catalytic subunit alpha-2
PRKACB	5567	protein kinase, cAMP-dependent, catalytic, beta
PRKACG	5568	protein kinase, cAMP-dependent, catalytic, gamma
PKLR	5313	pyruvate kinase, liver and RBC
PKM2	5315	pyruvate kinase, muscle
RIPK3	11035	receptor-interacting serine-threonine kinase 3
RYK	6259	RYK receptor-like tyrosine kinase
STK10	6793	serine/threonine kinase 10
STK11	6794	serine/threonine kinase 11
STK11IP	114790	serine/threonine kinase 11 interacting protein
STK16	8576	serine/threonine kinase 16
STK32A	202374	serine/threonine kinase 32A
SGK2	10110	serum/glucocorticoid regulated kinase 2
TBK1	29110	TANK-binding kinase 1
TSSK4	283629	testis-specific serine kinase 4
TTC33	23548	tetratricopeptide repeat domain 33
TGFBR1	7046	transforming growth factor, beta receptor 1
TPR	7175	translocated promoter region (to activated MET oncogene)
TRIB3	57761	tribbles homolog 3 (Drosophila)
TYK2	7297	tyrosine kinase 2

Table S4. Candidate list after the 2nd screen, related to Figure 6

- **manual counting**

Gene symbol	Gene ID	Gene name	Kinase type
AAK1	22848	AP2-associated kinase 1	Serine/threonine-protein kinase
ACVR2A	92	activin A receptor, type IIA	Serine/threonine-protein kinase
CAMKK2	10645	calcium/calmodulin-dependent protein kinase kinase 2, beta	Serine/threonine-protein kinase
CDC42BPA	8476	CDC42 binding protein kinase alpha (MRCK)	Serine/threonine-protein kinase
CERKL	375298	ceramide kinase-like	NAD kinase
CNKSR1	10256	connector enhancer of kinase suppressor of Ras 1	MAPK activation
FASTK	10922	Fas-activated serine/threonine kinase	Serine/threonine-protein kinase
GSG2	83903	germ cell associated 2 (haspin)	Serine/threonine-protein kinase
IRAK2	3656	interleukin-1 receptor-associated kinase 2	Serine/threonine-protein kinase
MAP3K7	6885	mitogen-activated protein kinase kinase kinase 7 (TAK1)	Serine/threonine-protein kinase
MAPK4	5596	mitogen-activated protein kinase 4 (ERK4)	Serine/threonine-protein kinase
MLKL	197259	mixed lineage kinase domain-like	Pseudokinase
NLK	51701	nemo-like kinase	Serine/threonine-protein kinase
PKLR	5313	pyruvate kinase, liver and RBC	pyruvate kinase
PKM2	5315	pyruvate kinase, muscle	pyruvate kinase, Serine/threonine-protein kinase
PRKAA2	5563	5'-AMP-activated protein kinase (AMPK) catalytic subunit alpha-2	Serine/threonine-protein kinase, Tyrosine kinase
RYK	6259	RYK receptor-like tyrosine kinase	Tyrosine kinase
TRIB3	57761	tribbles homolog 3 (Drosophila)	Protein kinase inhibition

Table S4. Candidate list after the 2nd screen, related to Figure 6 (continued)

- **software counting**

Gene symbol	Gene ID	Gene name	Kinase type
MAPK4	5596	mitogen-activated protein kinase 4 (ERK4)	Serine/threonine-protein kinase
PKLR	5313	pyruvate kinase, liver and RBC	pyruvate kinase
CNKSR1	10256	connector enhancer of kinase suppressor of Ras 1	MAPK activation
GSG2	83903	germ cell associated 2 (haspin)	Serine/threonine-protein kinase
RYK	6259	RYK receptor-like tyrosine kinase	Tyrosine kinase
RIPK3	11035	receptor-interacting serine-threonine kinase 3	Serine/threonine-protein kinase
PRKACB	5567	protein kinase, cAMP-dependent, catalytic, beta	Serine/threonine-protein kinase
PRKAA2	5563	5'-AMP-activated protein kinase (AMPK) catalytic subunit alpha-2	Serine/threonine-protein kinase
PKM2	5315	pyruvate kinase, muscle	Pyruvate kinase, Serine/threonine-protein kinase